Article

In-cell architecture of the nuclear pore and snapshots of its turnover

Check for updates

Matteo Allegretti[1,8], Christian E. Zimmerli[1,2,8], Vasileios Rantos[3], Florian Wilfling[4], Paolo Ronchi[5], Herman K. H. Fung[1], Chia-Wei Lee[4], Wim Hagen[1], Beata Turoňová[1], Kai Karius[3], Mandy Börmel[5], Xiaojie Zhang[1], Christoph W. Müller[1], Yannick Schwab[5,6], Julia Mahamid[1,6], Boris Pfander[4 ✉], Jan Kosinski[1,3 ✉] & Martin Beck[1,6,7 ✉]

Nuclear pore complexes (NPCs) fuse the inner and outer membranes of the nuclear envelope. They comprise hundreds of nucleoporins (Nups) that assemble into multiple subcomplexes and form large central channels for nucleocytoplasmic exchange[1,2]. How this architecture facilitates messenger RNA export, NPC biogenesis and turnover remains poorly understood. Here we combine in situ structural biology and integrative modelling with correlative light and electron microscopy and molecular perturbation to structurally analyse NPCs in intact *Saccharomyces cerevisiae* cells within the context of nuclear envelope remodelling. We find an in situ conformation and configuration of the Nup subcomplexes that was unexpected from the results of previous in vitro analyses. The configuration of the Nup159 complex appears critical to spatially accommodate its function as an mRNA export platform, and as a mediator of NPC turnover. The omega-shaped nuclear envelope herniae that accumulate in *nup116Δ* cells[3] conceal partially assembled NPCs lacking multiple subcomplexes, including the Nup159 complex. Under conditions of starvation, herniae of a second type are formed that cytoplasmically expose NPCs. These results point to a model of NPC turnover in which NPC-containing vesicles bud off from the nuclear envelope before degradation by the autophagy machinery. Our study emphasizes the importance of investigating the structure–function relationship of macromolecular complexes in their cellular context.

NPCs are giant macromolecular assemblies with an intricate architecture. About 30 different Nups assemble in multiple copies to form eight-fold rotationally symmetric NPCs, comprising approximately 550 protein building blocks in yeast[1]. The NPC consists of two outer rings, also called nuclear (NR) and cytoplasmic (CR) rings, which are located distally to the inner ring (IR). Scaffold Nups contain folded domains and form a cylindrical central channel. This channel is lined with FG Nups, which harbour intrinsically disordered Phe and Gly (FG)-rich repeats that interact with nuclear transport receptors. The Y-complex forms the outer rings, whereas the inner ring complex builds the IR[2]. The yeast Nup159 complex associates asymmetrically with the Y-complex at the CR and facilitates the terminal steps of mRNA export. Its core consists of two Nup159–Nup82–Nsp1 heterotrimers that dimerize into a characteristic P-shaped structure[4,5].

Genetic perturbation of Nup159 complex-associated Nup116[3] and Gle2[6] or nuclear envelope proteins such as Apq12[7] lead to the formation of clustered nuclear envelope herniae, omega-shaped morphologies that have been linked to neurological diseases such as dystonia[8,9]. Herniae engulf a membrane opening and contain Nups at their neck[3,9]; however, whether they engulf an entire or partial NPC remains unknown[10].

It has been suggested that herniae could be the result of inside-out assembly events of NPCs in which the fusion of the two nuclear membranes failed, or alternatively, the could comprise defective NPCs that were sealed off with membranes by the ESCRT machinery[10]. Recently, an autophagy pathway was described that degrades NPCs by direct interaction of the ubiquitin-like autophagosomal protein Atg8 with the cytosolic filament Nup159, which serves as an intrinsic autophagy receptor[11]. However, it remains unknown whether the formation of herniae is functionally related to the selective autophagy of NPCs.

Understanding how Nup subcomplexes are positioned relative to each other in cells requires the convergence of in vitro and in situ approaches[12]. In situ structural analysis is available for vertebrates and algae, and has revealed that key features of the NPC architecture are not conserved[1,13], such as the stoichiometry of Y-complexes within the outer rings. Notably, the P-shaped outline of the yeast Nup159 complex[5] was not apparent in any of the cryo-electron microscopy (cryo-EM) maps, suggesting either structural diversity, or questioning its physiological relevance.

There remains a lack of in situ structural analysis of the *S. cerevisiae* NPC, which has been extensively studied as a model organism for Nup

[1]Structural and Computational Biology Unit, European Molecular Biology Laboratory, Heidelberg, Germany. [2]Collaboration for joint PhD degree between EMBL and Heidelberg University, Faculty of Biosciences, Heidelberg, Germany. [3]Centre for Structural Systems Biology (CSSB), DESY and European Molecular Biology Laboratory, Hamburg, Germany. [4]Max Planck Institute of Biochemistry, Martinsried, Germany. [5]Electron Microscopy Core Facility (EMCF), European Molecular Biology Laboratory, Heidelberg, Germany. [6]Cell Biology and Biophysics Unit, European Molecular Biology Laboratory, Heidelberg, Germany. [7]Department of Molecular Sociology, Max Planck Institute of Biophysics, Frankfurt, Germany. [8]These authors contributed equally: Matteo Allegretti, Christian E. Zimmerli. ✉e-mail: bpfander@biochem.mpg.de; jan.kosinski@embl.de; martin.beck@biophys.mpg.de
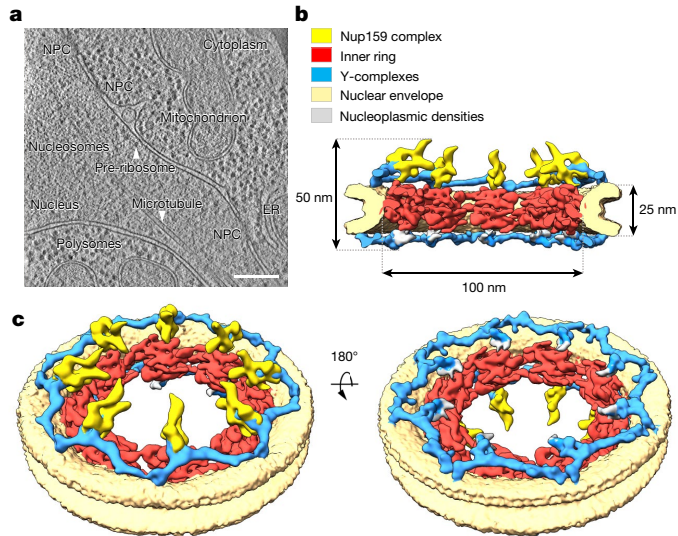
Fig. 1 | In-cell structure of _S. cerevisiae_ NPC. a, Cryo-tomographic slice of a _S. cerevisiae_ cell during division. _n_ = 240 tomograms of _S. cerevisiae_ wild-type cells were acquired from grids prepared on four different days from different cell cultures (biological replicates). ER, endoplasmic reticulum. Scale bar, 200 nm. **b**, Segmentation of the cryo-EM map of the _S. cerevisiae_ NPC cut in half along the central axis. **c**, Tilted view of the entire NPC showing both the cytoplasmic (left) and the nucleoplasmic (right) faces.

Fig. 2 | Nup159 complex architecture. a, Individual spoke of the NPC (colour-coded as in Fig. 1). The Nup159 complex is highlighted with a dotted frame. **b**, The Nup159 complex region of the in-cell NPC map (grey mesh) superimposed with the top-scoring systematic fit (see Methods) of the negative-stain map of the Nup159 complex[5] (yellow surface). **c**, Same as **b** but superimposed with the in-cell NPC map of a _nup116Δ_ strain grown at permissive temperature (yellow surface). **d**, Spatial model of how mRNA export is accommodated by the orientation of the Nup159 complex. A poly-A mRNA with transport factors Mex67–Mtr2 (red) and proteins that protect the poly-A tail from degradation (light green) docks to the unstructured region of the basket Nups[30] (grey box with blue filaments). The Nup159 N-terminal domain that mediates the release of the transport factors from the mRNA[31] is anchored at the cytoplasmic side.

structure, NPC architecture, biogenesis, surveillance and turnover, and the mechanism of mRNA export[1,11,14]. An integrative model of the entire _S. cerevisiae_ NPC architecture based on extensive experimental analysis in vitro has been recently put forward[15], but it remains unknown to what extent the native architecture of the NPC has been preserved.

Structure of the NPC in the cellular context

To characterize the architecture of _S. cerevisiae_ NPC in situ, we prepared thin cryo-focused ion beam (cryo-FIB) lamellae[16] of cells in the exponential growth phase. We acquired 240 cryo-electron tomograms (Fig. 1a) containing around 500 NPCs and determined the structure by subtomogram averaging. The resulting cryo-EM map at approximately 25 Å resolution (Extended Data Fig. 1a, b, Extended Data Table 1) provides a detailed overview of the native configuration and conformation of subcomplexes of actively transporting NPCs in cells (Fig. 1b, c, Extended Data Fig. 1b, c). A visual inspection of the structure reveals marked disparities, not only compared with the previously analysed structures of the algal[13] and human[17] NPCs, but also compared with previous analysis of isolated _S. cerevisiae_ NPC[15] (Extended Data Fig. 1c, d). With minor refinements, the integrative model of one asymmetric unit of the IR[15] fits unambiguously into the observed density ($P = 1.6 \times 10^{-12}$) (Extended Data Fig. 2), but the entire IR has to be dilated by about 20 nm in diameter, thereby spatially separating the eight individual spokes (Extended Data Fig. 3a). This analysis underlines the plasticity of the NPC within cells[13,16], which might be physiologically relevant for the transport of large cargos and inner nuclear membrane proteins.

As expected[15,18], 16 nuclear and cytoplasmic copies of the Y-complex are apparent in our cryo-EM map (Fig. 1c, d, Extended Data Fig. 1c). The crystal structures and homology models of the yeast Y-complex vertex[19] (Sec13–Nup145C–Nup84–Nup120–Seh1–Nup85) or its fragments fit into the observed Y-shaped density (Extended Data Fig. 2). We used an integrative modelling procedure taking into account the more extended in situ conformation and obtained complete structures of Y-complexes (Extended Data Fig. 3b, c, Supplementary Video 1). At the NR, additional densities appear at the connection to the IR and
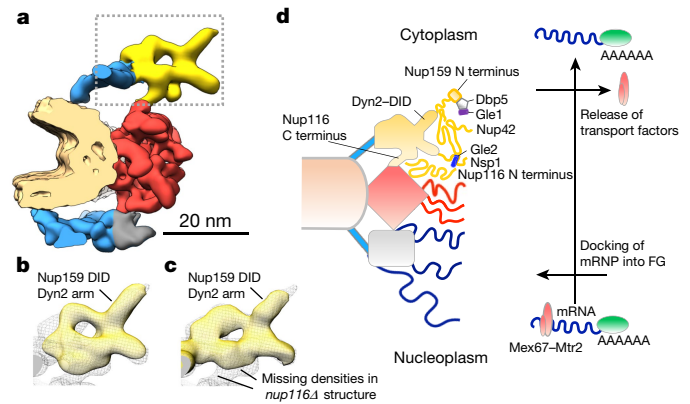
around the Y-complex, in particular after local masking (Figs. 1b, c, 2a, Extended Data Fig. 3d). The densities around the Y-complex form a rod that probably corresponds to fragments of the nuclear basket coiled-coil filaments as in the structure in ref. [15], but anchored to the Y-complex vertex.

A prominent feature of the electron microscopy map is the P-shaped density in the CR that is highly reminiscent of the previous analysis of the isolated, negatively stained Nup159 complex[4,5] (Fig. 2). Systematic fitting of the Nup159 complex negative-stain map[5] into our in situ structure confirmed this assignment (Fig. 2b, _P_ = 0.0027; Extended Data Fig. 4a). On the basis of the top resulting fit, we superimposed a representative integrative model of the Nup159 complex[4,15] and locally fitted it into our cryo-EM map (Extended Data Fig. 4b, Supplementary Video 1). The Nup82 β-propellers are positioned towards the inner ring, but nevertheless the previously published crosslinks[15] between the Nup159 and Y-complexes that map to the structure are satisfied (Extended Data Fig. 4e). The arm of the P-shape that consists of Nup159 DID tandem repeats binding multiple Dyn2 dimers[5,20] is clearly apparent in situ. In contrast to the previous model[15], it projects towards the cytoplasm at an angle of around 45° with respect to the nucleocytoplasmic axis (Fig. 2, Extended Data Fig. 4b).

nup116Δ confirms the orientation of Nup159 complex

Nup116 is one of the three yeast homologues of the essential vertebrate Nup98 and a key Nup for the NPC permeability barrier[21,22], mRNA export[21,23], pre-ribosome traslocation[24] and ring connectivity[15,25,26]. Superposition of the crystal structure[27] of Nup116(966–1111)–Nup82(1–452)–Nup159(1425–1458) with the respective parts of two copies of Nup159 and Nup82 contained in the P-complex (Extended Data Fig. 4c, d) suggested that the autoproteolytic domain of Nup116 is located in unassigned densities projecting towards the Nup188 in the IR. To validate this assignment, we structurally analysed the NPC in _nup116Δ_ cells at permissive temperature (25 °C, see Methods), at which NPCs have a normal morphological appearance[3]. The _nup116Δ_ structure is overall similar to the map of the wild type (Extended Data Fig. 6a, c,
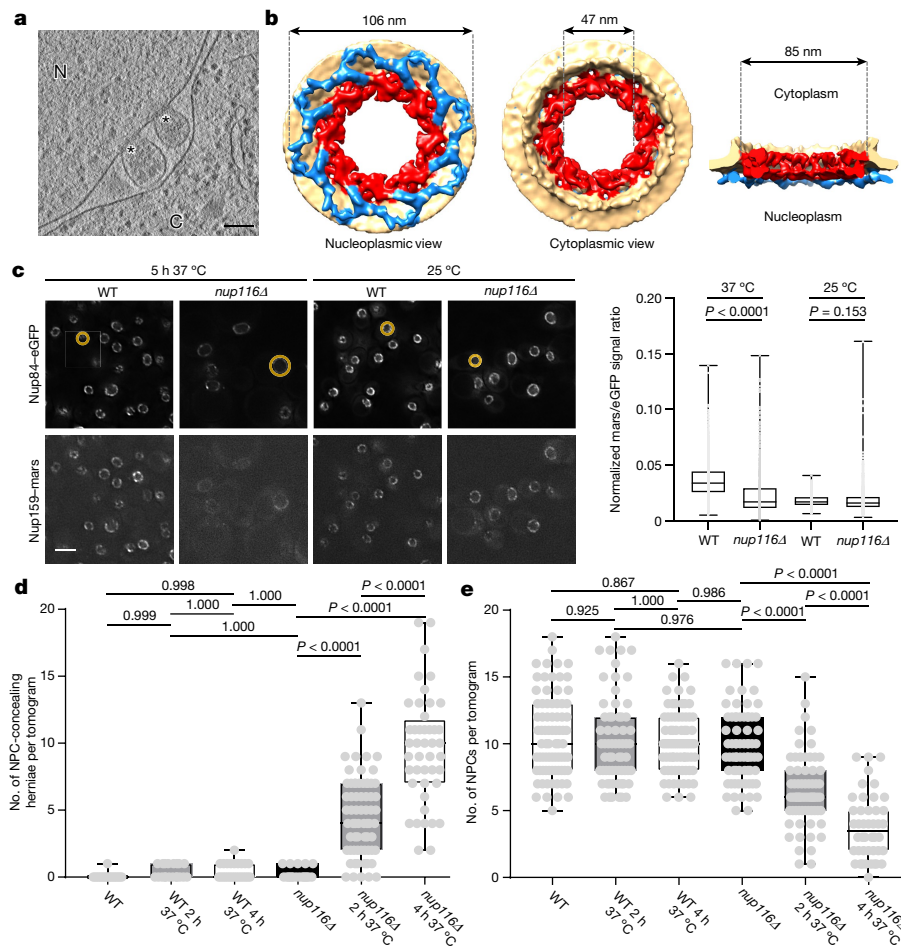
Fig. 3 | NPC-concealing hernia. a, Cryo-tomographic slice of a nuclear envelope with NPC-concealing herniae (*nup116Δ*, 4 h at 37 °C); N, nucleus; C, cytoplasm; asterisks mark densities at the neck of the herniae subjected to subtomogram averaging Scale bar, 100 nm. **b**, Segmentation of the cryo-EM map of the partial NPC found at the basis of NPC-concealing herniae. Colour code as in Fig. 1. **c**, Phase-contrast and maximum-intensity projections of deconvoluted wide-field microscopy stacks showing the nuclear envelope in wild-type (WT) and *nup116Δ* cells at 25 °C or 37 °C with markers Nup84 and Nup159. Yellow circles show the nuclear size (results quantified in Extended Data Fig. 6e). Right, the mars/eGFP ratio shows the significant loss of Nup159

signal in *nup116Δ* at 37 °C (three biologically independent replicates with *n* = 300 nuclei each, evaluated with Kruskal–Wallis test followed by Dunn's multiple comparisons test). **d**, Quantification of number of NPC-concealing herniae from 300 nm tomograms of *S. cerevisiae* cells (plastic sections) **e**, Quantification of number of NPCs not at the herniae from 300 nm tomograms acquired as in **d**. In **d**, **e**, *n* = 70 tomograms on average for each condition, see Supplementary Table 2; one-way ANOVA with Dunn's multiple comparisons test. In box plots (**c**–**e**), box centres are the median, box edges represent first and third quartiles and whiskers show minimum and maximum values.

Supplementary Video 2), but lacks density at the positions proximate to the Nup159 complex and Nup188 as predicted (Fig. 2c, Extended Data Fig. 4c). This finding corroborates the spatial positioning of Nup116 and the orientation of the Nup159 complex (Extended Data Fig. 5a, b). Previous crosslinking analysis[15] and biochemical data suggesting that Nup116 links to Nup188 and Nup192 of the IR[25,26] agree well with this configuration (Extended Data Figs. 4e, 5a, b). The position proximate to the SH3 domain of Nup188[28] in the NR also loses some density (Extended Data Figs. 5c, 6c, Supplementary Video 2), which would be in line with a cytoplasmically biased localization of Nup116[29].

Several studies have highlighted that the accurate positioning of the Nup159 complex with respect to the central channel at the cytoplasmic face of the NPC is critical for the spatial organization and directionality of mRNA export[4,30,31]. Our model of NPC architecture accommodates extensive biochemical analysis of mRNP export[21,30,31]. Indeed, Dbp5 and the N terminus of Nup159—which facilitate the terminal release of Mex67—are positioned towards the cytoplasm[32], whereas the FG repeats of Nsp1 that interact with Mex67 earlier during export, are placed towards the IR. (Fig. 2d). Nup159 itself also contains the Atg8-family interacting motif (AIM), which is located proximate to the

DID–Dyn2 arm and facilitates autophagic NPC turnover upon nitrogen starvation[11]. This AIM is exposed towards the cytosolic site, allowing access of Atg8 (Fig. 4a).

Herniae enclose partially assembled NPCs

Although the previous implications of the Nup159 complex in nuclear envelope herniae formation and selective autophagy suggest a functional link to membrane remodelling during NPC assembly and turnover, their exact relationship remains to be determined. We structurally analysed the membrane openings at the bases of the herniae formed in the *nup116Δ* strain at non-permissive temperature[5] (37 °C) (Fig. 3a, Supplementary Video 3) by subtomogram averaging (Fig. 3b, Extended Data Fig. 6a, b). We found that the necks of the herniae enclose partial NPCs that have a smaller diameter compared with the wild type (15 nm difference). Concurrently, the fused nuclear membranes are less curved (about 84° instead of 180°, on average; Fig. 3b, Extended Data Fig. 6a). The cryo-EM map reveals that the entire cytoplasmic ring, including the Nup159 and Y-complexes, and adjacent parts of the inner ring are missing (Fig. 3b, Extended Data Fig. 6a, c). Light microscopy data
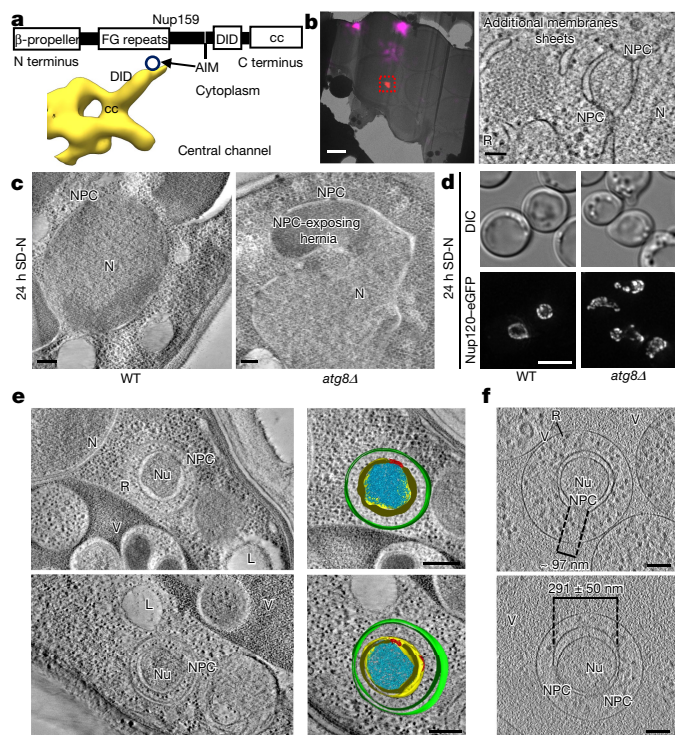
Fig. 4 | NPC-exposing hernia. a, Domain structure of Nup159 with corresponding region of the cryo-EM map showing the position of the Atg8-interacting motif (AIM[11]). cc, coiled coil domain. **b**, Three dimensional cryo-CLEM of Nup159–Atg8–split Venus (red) *nup120Δ* cells after 5.5 h of starvation, shown as cryo-EM overview of the lamella (left; scale bar, 2 μm; fiducials in magenta) and cryo-tomographic slice (right; relevant area framed red; scale bar, 100 nm). *n* = 2 tomograms were acquired in two independent sessions. R, ribosome. **c**, Tomographic slice from 300 nm plastic sections of wild-type and *atg8Δ S. cerevisiae* nuclei after 24 h of starvation (scale bar, 200 nm). *n* = 75 tomograms of independent nuclei (technical replicates) were acquired. SD-N, synthetic minimal medium lacking nitrogen. **d**, Phase-contrast and deconvoluted wide-field maximum-intensity projection of the same strains imaged live before and after 24 h of starvation (three biologically independent replicates and *n* = 300 per replica). **e**, Tomographic slice (plastic section), corresponding segmentation and isosurface rendering of NPC-containing nuclear vesicles in the cytoplasm from *S. cerevisiae atg15Δ* cells starved for approximately 24 h. Vesicles are surrounded by ribosomes and two membranes. Nuclear content (Nu) in cyan, double membrane in green. V, vacuole; L, lipid droplet. *n* = 5 tomograms from different cells (technical replicates) were acquired. Scale bar, 200 nm. **f**, Cryo-tomographic slices of NPC-containing nuclear vesicles in the vacuole from *S. cerevisiae atg15Δ* cells starved for 24 h. The vesicles are surrounded by ribosomes and only one membrane. Scale bar, 100 nm. *n* = 35 vesicles (technical replicates) show an NPC diameter of 97.4 ± 6.5 nm and a nuclear vesicle diameter of 291 ± 50 nm (mean ± s.d.).

confirm that the Nup159 complex fails to integrate into NPCs under these conditions (Fig. 3c). Quantification of the tomographic electron microscopy data revealed that in *nup116Δ* cells at 37 °C, herniae accumulate over time at the nuclear envelope concomitantly with a decrease of non-herniated NPCs (Fig. 3d, e). Even at permissive temperature (25 °C) the nuclear envelope of *nup116Δ* cells in our cryo-tomograms contain a significantly increased number of mushroom-shaped evaginations of the inner nuclear membrane (Extended Data Fig. 6d). This nuclear envelope morphology is reminiscent of interphase assembly intermediates in human cells[33].

Three different lines of evidence, (1) the appearance of evaginations, (2) the fact that partial NPCs are enclosed in herniae, and (3) the interdependence of herniae and NPC number, strongly support models that

conceptualize herniae as a consequence of failed, inside-out interphase assembly[34]. They point to a direct or indirect contribution of Nup116 to the fusion of the two nuclear membranes during NPC assembly that if compromised, prevents the association of the cytoplasmic NPC components. Although herniae should not be conceived as 'on-pathway' intermediates of NPC assembly, some Nup interactions relevant for NPC biogenesis might be preserved. We built the structural model refining the WT *S. cerevisiae* NPC model into this map (Supplementary Video 4), which confirms that only the Y-complexes of the NR and partial IR are confidently assigned. The Y-complexes of the NR take up a conformation in which the Nup85 arm contacts the IR in the Nic96 region, forming a continuous coat across NR and IR[35] that was not observed in any of the previously published NPC structures (Extended Data Fig. 6c, Supplementary Video 4).

NPC-exposing herniae are subject to autophagy

The reduction of functionally assembled NPCs under *nup116Δ* conditions is concurrent with an increased nuclear size[3] (Extended Data Fig. 6e, f), emphasizing the association between the accumulation of the herniae, a consequent defective nuclear transport activity and nuclear size control[36]. Since binding of Atg8 to Nup159 is an essential prerequisite for autophagic clearance of NPCs, our structural analysis predicts that herniae of *nup116Δ* cells shifted to non-permissive temperature cannot be cleared by selective autophagy because their NPCs are not accessible to the cytoplasm and they do not include the AIM-containing Nup159 complex (Fig. 3a, b, Extended Data Fig. 6a, Supplementary Videos 3–4). Indeed, the degradation of NPCs upon nitrogen starvation was strongly reduced in *nup116Δ* cells at 30 °C as compared to 25 °C (Extended Data Fig. 7a).

To investigate how the autophagy machinery is recruited to the NPC, we used a split-Venus approach to visualize the Nup159–Atg8 interaction[11] (Extended Data Fig. 8a) using correlative light and electron microscopy[37,38] (CLEM) in an NPC-clustering background (*nup120Δ*[11]) that was shown to induce hernia-related structures in which many NPCs are cytoplasmically exposed[39]. After 5.5 h of nitrogen starvation, we identified the regions of interest (Fig. 4b, Extended Data Fig. 8b) and acquired electron tomograms at positions of NPCs engaged in Atg8 interaction. Although interaction between receptors and Atg8 does not require prior lipidation of Atg8 to the phagophore[40,41], these data revealed agglomerates of herniae similar to those described in ref. [39], surrounded by additional membrane sheets (Fig. 4b, Extended Data Fig. 8b, Supplementary Videos 5, 8–10). These additional membranes were seen in several but not all tomograms, which is expected, given the transient nature of this intermediate of the autophagy pathway. Nevertheless, the structures we observed were often connected to the nuclear envelope and may represent endoplasmic reticulum that contributes to isolation-membrane formation[42–44]. As expected, under these conditions, herniae expose NPCs to the cytosol and thus the AIM motifs are accessible to the selective autophagy machinery. We therefore distinguish between 'NPC-concealing herniae', Ω-shaped nuclear envelope morphologies observed under *nup116Δ* conditions at 37 °C, and 'NPC-exposing herniae', nuclear membrane blebs that cytoplasmically expose NPCs containing the Nup159 complex, as observed under *nup120Δ* conditions.

To clarify whether 'NPC-exposing herniae' are typical for selective autophagy of NPCs during nitrogen starvation or rather a peculiarity of the *nup120Δ*, we analysed *atg8Δ* cells in which the respective autophagy machinery cannot be recruited to the NPC and Nup degradation by autophagy is inhibited. Under these conditions, we observed a prominent accumulation of deformed nuclei (Fig. 4c, d, Extended Data Fig. 7c, d) with larger NPC-exposing herniae compared with *nup120Δ*; NPCs were mildly clustered (Extended Data Fig. 7e) and very dense material accumulated inside them (Supplementary Video 6). A considerably less pronounced phenotype was observed upon interference with the

Article

ESCRT machinery[45] (Extended Data Fig. 7b, f). Together, our results support a model in which NPC-exposing herniae accumulate at the nuclear envelope under conditions in which selective autophagy is triggered (nitrogen starvation), but the autophagy machinery is missing (Fig. 4c, d, Extended Data Fig. 7b–d, f, g). This model predicts that a piece of the nuclear envelope containing clustered NPCs buds off into cytoplasmic intermediates of NPC degradation. To test this prediction, we analysed *atg15Δ* cells in which lipid degradation in the vacuole is perturbed[11]. Indeed, NPC-containing nuclear vesicles surrounded by ribosomes and double membranes typical of autophagosomes were observed in the cytosol, disconnected from the nuclear envelope (Fig. 4e, Supplementary Video 7). They are also found in the vacuole, as shown in ref. [11], surrounded by a single membrane. Cryo-ET analysis revealed that the diameter of NPCs contained in such nuclear vesicles is similar to those in the wild type (Fig. 4f).

Conclusions

Our in situ structural analysis of the *S. cerevisiae* NPC highlights the physiological relevance of the orientation of the Nup159 complex with respect to the NPC scaffold, which accommodates the terminal steps of mRNA export and enables the exposure of the intrinsic AIM. Indeed, our data suggest that the accessibility of the Nup159 complex at the NPC-exposing hernia is critical for nuclear envelope budding and selective autophagy of NPCs, whereas NPC-concealing herniae are probably a result of failed NPC assembly (Extended Data Fig. 9), although some of the individual steps need to be investigated in more detail. Whether the material contained in the NPC-containing vesicles and NPC-exposing herniae can be attributed to specific cargos or is simply unspecific nuclear content remains to be determined. Our structural models of the WT and *nup116Δ S. cerevisiae* NPC reveal conformational changes and interactions previously unobserved in NPC structures, suggesting that NPC assembly might be facilitated by dedicated Nup interactions between the NR and the IR, which require further investigation. Finally, our findings highlight the power of in-cell cryo-EM to provide insights into fundamental processes of eukaryotic cell biology.

Online content

Any methods, additional references, Nature Research reporting summaries, source data, extended data, supplementary information, acknowledgements, peer review information; details of author contributions and competing interests; and statements of data and code availability are available at https://doi.org/10.1038/s41586-020-2670-5.

1. Lin, D. H. & Hoelz, A. The structure of the nuclear pore complex (an update). *Annu. Rev. Biochem.* **88**, 725–783 (2019).
2. Beck, M. & Hurt, E. The nuclear pore complex: understanding its function through structural insight. *Nat. Rev. Mol. Cell Biol.* **18**, 73–89 (2017).
3. Wente, S. R. & Blobel, G. A temperature-sensitive NUP116 null mutant forms a nuclear envelope seal over the yeast nuclear pore complex thereby blocking nucleocytoplasmic traffic. *J. Cell Biol.* **123**, 275–284 (1993).
4. Fernandez-Martinez, J. et al. Structure and function of the nuclear pore complex cytoplasmic mRNA export platform. *Cell* **167**, 1215–1228 (2016).
5. Gaik, M. et al. Structural basis for assembly and function of the Nup82 complex in the nuclear pore scaffold. *J. Cell Biol.* **208**, 283–297 (2015).
6. Murphy, R., Watkins, J. L. & Wente, S. R. GLE2, a *Saccharomyces cerevisiae* homologue of the *Schizosaccharomyces pombe* export factor RAE1, is required for nuclear pore complex structure and function. *Mol. Biol. Cell* **7**, 1921–1937 (1996).
7. Scarcelli, J. J., Hodge, C. A. & Cole, C. N. The yeast integral membrane protein Apq12 potentially links membrane dynamics to assembly of nuclear pore complexes. *J. Cell Biol.* **178**, 799–812 (2007).
8. Pappas, S. S., Liang, C. C., Kim, S., Rivera, C. O. & Dauer, W. T. TorsinA dysfunction causes persistent neuronal nuclear pore defects. *Hum. Mol. Genet.* **27**, 407–420 (2018).
9. Laudermilch, E. et al. Dissecting Torsin/cofactor function at the nuclear envelope: a genetic study. *Mol. Biol. Cell* **27**, 3964–3971 (2016).
10. Thaller, D. J. & Patrick Lusk, C. Fantastic nuclear envelope herniations and where to find them. *Biochem. Soc. Trans.* **46**, 877–889 (2018).
11. Lee, C.-W. et al. Selective autophagy degrades nuclear pore complexes. *Nat. Cell Biol.* **22**, 159–166 (2020).
12. Hoelz, A., Glavy, J. S. & Beck, M. Toward the atomic structure of the nuclear pore complex: when top down meets bottom up. *Nat. Struct. Mol. Biol.* **23**, 624–630 (2016).
13. Mosalaganti, S. et al. In situ architecture of the algal nuclear pore complex. *Nat. Commun.* **9**, 2361 (2018).
14. Ungricht, R. & Kutay, U. Mechanisms and functions of nuclear envelope remodelling. *Nat. Rev. Mol. Cell Biol.* **18**, 229–245 (2017).
15. Kim, S. J. et al. Integrative structure and functional anatomy of a nuclear pore complex. *Nature* **555**, 475–482 (2018).
16. Mahamid, J. et al. Visualizing the molecular sociology at the HeLa cell nuclear periphery. *Science* **351**, 969–972 (2016).
17. von Appen, A. et al. In situ structural analysis of the human nuclear pore complex. *Nature* **526**, 140–143 (2015).
18. Rajoo, S., Vallotton, P., Onischenko, E. & Weis, K. Stoichiometry and compositional plasticity of the yeast nuclear pore complex revealed by quantitative fluorescence microscopy. *Proc. Natl Acad. Sci. USA* **115**, E3969–E3977 (2018).
19. Stuwe, T. et al. Nuclear pores. Architecture of the nuclear pore complex coat. *Science* **347**, 1148–1152 (2015).
20. Stelter, P. et al. Molecular basis for the functional interaction of dynein light chain with the nuclear-pore complex. *Nat. Cell Biol.* **9**, 788–796 (2007).
21. Strawn, L. A., Shen, T. & Wente, S. R. The GLFG regions of Nup116p and Nup100p serve as binding sites for both Kap95p and Mex67p at the nuclear pore complex. *J. Biol. Chem.* **276**, 6445–6452 (2001).
22. Schmidt, H. B. & Görlich, D. Nup98 FG domains from diverse species spontaneously phase-separate into particles with nuclear pore-like permselectivity. *eLife* **4**, e04251 (2015).
23. Adams, R. L., Terry, L. J. & Wente, S. R. Nucleoporin FG domains facilitate mRNP remodeling at the cytoplasmic face of the nuclear pore complex. *Genetics* **197**, 1213–1224 (2014).
24. Stage-Zimmermann, T., Schmidt, U. & Silver, P. A. Factors affecting nuclear export of the 60S ribosomal subunit in vivo. *Mol. Biol. Cell* **11**, 3777–3789 (2000).
25. Fischer, J., Teimer, R., Amlacher, S., Kunze, R. & Hurt, E. Linker Nups connect the nuclear pore complex inner ring with the outer ring and transport channel. *Nat. Struct. Mol. Biol.* **22**, 774–781 (2015).
26. Onischenko, E. et al. Natively unfolded FG repeats stabilize the structure of the nuclear pore complex. *Cell* **171**, 904–917.e19 (2017).
27. Yoshida, K., Seo, H.-S., Debler, E. W., Blobel, G. & Hoelz, A. Structural and functional analysis of an essential nucleoporin heterotrimer on the cytoplasmic face of the nuclear pore complex. *Proc. Natl Acad. Sci. USA* **108**, 16571–16576 (2011).
28. Andersen, K. R. et al. Scaffold nucleoporins Nup188 and Nup192 share structural and functional properties with nuclear transport receptors. *eLife* **2**, e00745 (2013).
29. Rout, M. P. et al. The yeast nuclear pore complex: composition, architecture, and transport mechanism. *J. Cell Biol.* **148**, 635–652 (2000).
30. Terry, L. J. & Wente, S. R. Nuclear mRNA export requires specific FG nucleoporins for translocation through the nuclear pore complex. *J. Cell Biol.* **178**, 1121–1132 (2007).
31. Weirich, C. S., Erzberger, J. P., Berger, J. M. & Weis, K. The N-terminal domain of Nup159 forms a β-propeller that functions in mRNA export by tethering the helicase Dbp5 to the nuclear pore complex. *Mol. Cell* **16**, 749–760 (2004).
32. Vallotton, P. et al. Mapping the native organization of the yeast nuclear pore complex using nuclear radial intensity measurements. *Proc. Natl Acad. Sci. USA* **116**, 14606–14613 (2019).
33. Otsuka, S. et al. Nuclear pore assembly proceeds by an inside-out extrusion of the nuclear envelope. *eLife* **5**, e19071 (2016).
34. Zhang, W. et al. Brr6 and Brl1 locate to nuclear pore complex assembly sites to promote their biogenesis. *J. Cell Biol.* **217**, 877–894 (2018).
35. Beck, M., Mosalaganti, S. & Kosinski, J. From the resolution revolution to evolution: structural insights into the evolutionary relationships between vesicle coats and the nuclear pore. *Curr. Opin. Struct. Biol.* **52**, 32–40 (2018).
36. Cantwell, H. & Nurse, P. Unravelling nuclear size control. *Curr. Genet.* **65**, 1281–1285 (2019).
37. Kukulski, W. et al. Correlated fluorescence and 3D electron microscopy with high sensitivity and spatial precision. *J. Cell Biol.* **192**, 111–119 (2011).
38. Arnold, J. et al. Site-specific cryo-focused ion beam sample preparation guided by 3D correlative microscopy. *Biophys. J.* **110**, 860–869 (2016).
39. Aitchison, J. D., Blobel, G. & Rout, M. P. Nup120p: a yeast nucleoporin required for NPC distribution and mRNA transport. *J. Cell Biol.* **131**, 1659–1675 (1995).
40. Shvets, E., Abada, A., Weidberg, H. & Elazar, Z. Dissecting the involvement of LC3B and GATE-16 in p62 recruitment into autophagosomes. *Autophagy* **7**, 683–688 (2011).
41. Sawa-Makarska, J. et al. Cargo binding to Atg19 unmasks additional Atg8 binding sites to mediate membrane-cargo apposition during selective autophagy. *Nat. Cell Biol.* **16**, 425–433 (2014).
42. Osawa, T. et al. Atg2 mediates direct lipid transfer between membranes for autophagosome formation. *Nat. Struct. Mol. Biol.* **26**, 281–288 (2019).
43. Schütter, M., Giavalisco, P., Brodesser, S. & Graef, M. Local fatty acid channeling into phospholipid synthesis drives phagophore expansion during autophagy. *Cell* **180**, 135–149 (2020).
44. Valverde, D. P. et al. ATG2 transports lipids to promote autophagosome biogenesis. *J. Cell Biol.* **218**, 1787–1798 (2019).
45. Thaller, D. J. et al. An ESCRT–LEM protein surveillance system is poised to directly monitor the nuclear envelope and nuclear transport system. *eLife* **8**, e45284 (2019).

Methods

Data reporting
No statistical methods were used to predetermine sample size. The experiments were not randomized. The investigators were not blinded to allocation during experiments and outcome assessment.

Yeast strains, growth conditions, fluorescence imaging
Strains used in this study are listed in Supplementary Table 1. Genotypes were verified using PCR and by selectable markers. Cells were grown at indicated temperatures (25 °C, 30 °C and 37 °C) to mid-log phase in YPAD (1% yeast extract, 2% peptone, 0.04% adenine, 2% dextrose). Nitrogen starvation was carried out by switching cells grown at OD_{600} ~0.5 with YPAD into synthetic minimal medium lacking nitrogen (SD-N medium) (0.17% yeast nitrogen base, without amino acids and ammonium sulfate, supplemented with 2% glucose) for indicated times.

Fluorescence microscopy
For fluorescence microscopy, yeast cells were grown in low-fluorescence synthetic growth medium (yeast nitrogen base without amino acids and without folic acid and riboflavin (FORMEDIUM)) supplemented with all essential amino acids and 2% glucose. The next day, cells were diluted to OD 0.1 and grown to mid log phase (0.5–0.8 OD) before imaging. Microscopy slides were pretreated with 1 mg ml⁻¹ concanavalin A (ConA) solution. The wide-field imaging was performed at the Imaging Facility of the Max Planck Institute of Biochemistry (MPIB-IF) on a GE DeltaVision Elite system based on an OLYMPUS IX-71 inverted microscope, an OLYMPUS (100× 1.40 NA UPLSAPO and 60× 1.42 NA PLAPON) objective and a PCO sCMOS 5.5 camera. Images were deconvolved using the softWoRx Software (default values except: method, additive enhanced, 20 iterations). For Extended Data Fig. 8a, images were acquired using a wide-field fluorescence microscope (Olympus IX81) equipped with an Olympus PlanApo 100× 1.40 NA oil-immersion objective and a CCD camera (Orca-ER; Hamamatsu Photonics). All light microscopy figures were analysed in FIJI[46]. For quantifying nuclear size fold increase in Extended Data Fig. 6e, round nuclei from maximum-intensity projections were circled as shown in Fig. 3c to calculate area and the radius (r) using FIJI. The volume was extrapolated using the formula $(4/3) \times \pi r^3$. For fluorescent intensity quantifications in Extended Data Fig. 8a, cell background was subtracted from each intensity measurement.

Immunoblot techniques
We collected 3×10^7 cells (OD 1.5) at 25 °C and 30 °C (at 37 °C the *nup116Δ* strain is not viable under starvation conditions) for the indicated time points, and total cell protein extracts were obtained using alkaline lysis (2 M NaOH and 7.5% (v/v) 2-mercaptoethanol for 15 min on ice) followed by trichloroacetic acid precipitation (to a final concentration of 22% for 10 min on ice). Protein pellets were collected by centrifugation (14,000 rpm, 20 min), solubilized in HU loading buffer (8 M urea, 5% SDS, 200 mM Tris-HCl pH 6.8, 20 mM dithiothreitol and 1.5 mM bromophenol blue) and disrupted by vortexing with an equal volume of acid-washed glass beads (425–600 μm) for 6 min. The samples were then incubated at 65 °C (1,400 rpm) for 10 min. Proteins were separated using NuPAGE 4–12% gradient gels (Invitrogen), transferred onto polyvinylidene fluoride membranes (Immobilon-P) and then analysed using the specific antibodies. Monoclonal antibody against Dpm1 (1:10,000; clone 5C5A7) was purchased from Invitrogen. The monoclonal GFP antibody (1:500; clone B-2) was purchased from Santa Cruz Biotechnology. To calculate degradation of eGFP-fused protein levels (%), the intensity of the full-length eGFP-fused protein was normalized to the intensity of the respective loading control, and shown as relative to wild-type cells at 0 h. To calculate degradation of eGFP′ (eGFP resistant to vacuolar degradation) levels (fold change), the intensity of the free eGFP′ was divided by the intensity of the Dpm1 loading control; values are shown relative to that in WT cells (always normalized to the longest starvation time point of the WT cells).

Correlative fluorescence and electron tomography in plastic sections
CLEM analysis was conducted as previously described[37,45]. *S. cerevisiae* cells were high-pressure frozen after ~5 h of starvation (HPM010, Abra-Fluid) and freeze substituted (EM-AFS2, Leica) with 0.1% uranyl acetate in acetone for 55 h at −90 °C. The temperature was then increased to −45 °C at 3.5 °C h⁻¹ and samples were further incubated for 5 h. After rinsing in acetone, the samples were infiltrated in Lowicryl HM20 and the resin was polymerized under UV light. Sections 300 nm thick were cut with a microtome (EM UC7, Leica) and placed on carbon coated 200 mesh copper grids (S160, Plano). The fluorescence microscopy imaging of the sections was carried out as previously described[45,47] using a wide-field fluorescence microscope (Olympus IX81) equipped with an Olympus PlanApo 100× 1.40 NA oil-immersion objective and a CCD camera (Orca-ER; Hamamatsu Photonics). After fluorescence imaging, grids were post-stained with uranyl acetate and lead citrate. Protein A-coupled gold beads (15 nm) were also added as fiducial markers used for overlaying low-mag with high-mag tomograms. Tilt series of the cells of interest (60° to 60°) were acquired semi-automatically on a Tecnai F30 (Thermofisher, FEI) at 300 kV with Serial-EM[48] at 20,000× and at 4,700× to facilitate ease of correlation. Tomograms were reconstructed automatically with IMOD batchruntomo[49]. Tilts were aligned by patch tracking. IMOD[49] was used for manual segmentation of the tomograms. Overlays of fluorescence spots and tomograms was performed with the ec-CLEM Plugin[50] in ICY[51] by clicking manually on corresponding pairs of notable features in the two imaging modalities.

2D and 3D electron microscopy
S. cerevisiae cells upon starvation were high-pressure frozen as described above and freeze substituted with 0.2% uranyl acetate 0.1% glutaraldehyde in acetone for 60 h at −90 °C. The temperature was then increased to −45 °C at 3 °C h⁻¹ and samples were further incubated for 9 h. After rinsing in acetone, the samples were infiltrated in Lowicryl HM20 resin and the resin was polymerized under UV light. Grids were poststained as described above. Acquisition was performed with a Tecnai F30 (Thermofisher, FEI) at 300 kV. NPC-concealing hernia, NPCs and NPC-exposing hernia counting was performed using 3D tomographic volumes after acquisition of tilt-series from 300-nm sections with Serial EM[48]. See Supplementary Table 2 for number of tomograms for each strain. Box plots were drawn with Graphpad Prism 6.0. For NPC density calculations (NPCs per μm²), nuclear surface was calculated in IMOD[49] after nuclei segmentation.

Cryo-FIB milling and cryo-CLEM
S. cerevisiae strains were grown in YPAD liquid medium to an OD_{600} of 0.2 at 30 °C, then transferred to SD-N liquid medium or to a 37 °C incubator accordingly. Per grid, 3.5 μl of cell suspension were applied on 200 mesh copper grids coated with R 2/1 holey carbon or SiO₂ films (Quantifoil Micro Tools) and plunge frozen in liquid ethane at ~−186 °C using a Leica EM GP grid plunger. The blotting chamber conditions were adjusted to 30 °C, 95% humidity and 1.5–2 s blotting time. For cryo-CLEM, Crimson FluoSpheres Carboxylate-Modified Microspheres, 1.0 μm, Crimson fluorescent (625/645), were washed in 1× PBS and added to the cell suspension at 1:20 dilution, and 1 s blotting time was used. The frozen grids were fixed in modified autogrids to allow milling at a shallow angle[52] and transferred into an Aquilos (cryo-FIB-SEM dual beam, Thermofisher). For correlative studies, the clipped grids were imaged on a prototype Leica cryo-confocal microscope based on Leica TCS SP8 CFS equipped with a Cryo Stage (similar to the commercially available EM Cryo CLEM Widefield system). Imaging was performed using a 50× objective, NA 0.90, 552-nm laser excitation, and detecting simultaneously at 560–620 nm and 735–740 nm. In the Aquilos, samples were sputter-coated with inorganic platinum and coated with an organometallic protective platinum layer using the Aquilos gas-injection

Article

system[53]. Lamellae were produced using the Gallium ion beam at 30 kV and stage tilt angles of 17°–19° by milling in two parallel rectangular patterns. The lamella preparation was conducted in a stepwise fashion, gradually reducing the current of the ion beam until the final polishing of a thin slab of biological material of around 150–250 nm. For correlative studies, beads (5 to 10) were picked in the squares of interested and overlaid with fluorescence signals coming from the confocal stacks using 3DCT in both the electron and ion beam images[38]. After choosing the signal of interest in the confocal stacks, 3DCT provides the position to place the milling patterns in x, y and z coordinates. Milling is then performed as described above after choosing grid squares with intact film. After polishing, the signal of interest is retained in the lamellae. Autogrids with lamellae were unloaded and placed in storage boxes. In some cases, a further inorganic platinum layer was added to reduce charging during transmission electron microscopy imaging.

Cryo-electron tomography data collection and processing
Grids with lamellae were loaded into the Krios cassette. Cryo-electron tomographic tilt series (TS) were acquired on a Titan Krios (Thermofisher FEI) operating at 300 kV equipped with a Gatan K2 summit direct electron detector and energy filter. The autogrids were carefully loaded with the lamella orientation perpendicular to the tilt-axis of the microscope before TS acquisition. Lamellae were mapped at low mag (2 nm per pixel, 30 kV slit) and for correlative studies the maps were overlaid with the electron beam images from the Aquilos using serial EM registration points. Spots of interested were chosen accordingly. All data was collected using the K2 operating in dose-fractionation mode at 4k × 4k resolution with a nominal pixel size of 0.34 nm. TS collection was automated at using a modified version of the dose-symmetric scheme[54] taking the lamella pre-tilt into account. Defocus TS were acquired over a tilt range of +65 to −45 for a positive pre-tilt with a tilt increment of 2–3°, a total dose of ~140 e^- A^{-2} and a targeted defocus of around 2 to 4.5 μm.

All images were pre-processed and dose-filtered as described in[55]. Tilt-series alignment was performed using IMOD software package 4.9.2[49], by patch tracking function on bin4 image stacks. Initial tilt series alignment was manually inspected and improved by removing contours showing large deviations (that is, a large mean residual error) from the alignment model function. The software package gCTF[56] was used for CTF estimation. The 3dCTF correction and tomogram reconstruction was performed with NovaCTF[57].

Subtomogram alignment and averaging
Subtomogram alignment and averaging was performed with slight modifications from a previously described workflow[58] using the Matlab TOM package re-implemented in C++. In brief, particle coordinates and initial orientations were manually picked and assigned. Initial NPC alignment was performed on 8 and 4 times binned subtomograms followed by a manual inspection and curation of the initial alignment for each particle. From the whole aligned NPCs all 8 spokes were assigned according to an eightfold rotational symmetry and the subunits were extracted from the tomograms removing subunits which are located outside of the lamellae. Subunits were further aligned. The alignment was once more manually inspected and all misaligned subunits were removed. Final alignments were done binning two times the subtomograms using focused masks on the cytoplasmic, inner and nucleoplasmic ring of the NPC. In the *S. cerevisiae* wild-type dataset ~500 NPCs (4,000 asymmetric units) were initially picked from ~240 tomograms, ~250 NPCs (2,000 asymmetric units) from 145 tomograms for the *nup116Δ* strain at permissive temperature and ~60 NPCs from ~70 tomograms for the *nup116Δ* strain at not-permissive temperature (37 °C). The particles were split in two half datasets for gold-standard processing. After alignment and manual curation ~2,000 subunits were used in the final average for the wild-type NPC and ~1,300 for the *nup116Δ* at permissive temperature and 450 for the *nup116Δ* strain at

37 °C. For the latter NPCs, SIRT-like filtered volumes generated with IMOD[49] were used for alignment and weighted back projection volumes to get the final structure. Gold standard Fourier shell correlation (FSC) was calculated with the Fourier shell correlation server (www.ebi.ac.uk/pdbe/emdb/validation/fsc/results/) with half-maps as inputs. Local resolution was calculated with Resmap[59], B-factor sharpening was estimated empirically as in ref.[17]. Difference maps were calculated using USCF Chimera[60].

Systematic fitting of NPC components to the cryo-ET map
An unbiased systematic (global) fitting approach was performed using structural models of various *S. cerevisiae* NPC subcomplexes derived from previously published structures[3,15]. All structural models were low-pass filtered to 40 Å prior the fitting. The resulting model maps were then independently fitted into the NPC cryo-EM map from this study using global fitting as implemented in UCSF Chimera[60]. The fitting of the Y-complex structures and Nup159 complex was performed for CR and NR segments of the in-cell cryo-EM NPC map. The nuclear envelope density was erased before the fitting with the tool 'volume eraser' from UCSF Chimera[60]. The regions of the nuclear envelope distant from apparent contact points between membrane and protein densities were erased before the fitting to eliminate fits overlapping with the membrane. All fitting runs were performed using 100,000 random initial placements and the requirement of at least 30% of the model map to be covered by the NPC density envelope from this study defined at low threshold. For each fitted model, this procedure yielded between 500 and 17,000 fits with unique conformation after clustering.

For fitting the filtered atomic models, the cross-correlation about the mean (cam score, equivalent to Pearson correlation) score from UCSF Chimera[60] was used as a fitting metric as in our previous works[13,17,55]:

$$cam = \frac{\langle \mathbf{u} - \mathbf{u}_{ave}, \mathbf{v} - \mathbf{v}_{ave} \rangle}{|\mathbf{u} - \mathbf{u}_{ave}||\mathbf{v} - \mathbf{v}_{ave}|}$$

where $\mathbf{u}_{ave}$ is a vector with all components equal to the average of the components of $\mathbf{u}$ and $\mathbf{v}_{ave}$ is defined analogously.

The negative-stain map of the Nup159 complex was fitted using UCSF Chimera's cross-correlation about zero (equivalent to cosine similarity) score (cc):

$$cc = \frac{\langle \mathbf{u}, \mathbf{v} \rangle}{|\mathbf{u}||\mathbf{v}|}$$

This score was used instead of the cam score since the cam score tests the linear dependence of the two fitted maps, which is not the case when fitting negative-stain maps, which contain the signal of the electron density at the surface of the complex.

The Nup159 complex was also fitted using the Colores program from the Situs package[61] with settings appropriate for low-resolution negative-stain maps (that is, using Laplacian filtering that emphasizes on contour matching over interior volume matching).

For each fitting run, the statistical significance of the fits was assessed as a P value calculated from the normalized cross-correlation scores. To calculate the P values, the cross-correlation scores were first transformed to z-scores (Fisher's z-transform) and centred, from which two-sided P values were computed using standard deviation derived from an empirical null distribution (derived from all obtained unique fits and fitted using fdrtool[62] R-package). All P values were corrected for multiple testing using Benjamini–Hochberg procedure[63]. Figures were made using UCSF Chimera[60] and Xlink Analyzer[64].

Integrative modelling
To build the integrative model of *S. cerevisiae* NPC, the IR model from ref.[15] was first fitted as a rigid body using the procedure described above (systematic fitting). The fit was statistically significant but

was nevertheless further refined to optimize the fitting of individual domains. For the refinement, the structure of the IR was divided into rigid bodies corresponding to the original crystal structures used as modelling templates from ref. [15] and the positions of the rigid bodies were optimized using a custom refinement protocol implemented with Integrative Modelling Platform (IMP)[65] v.2.12.0, similar to the procedure used in ref. [66]. The protocol employs a Monte Carlo simulated annealing optimization of the rigid bodies' rotations and translations and an integrative scoring function, which consisted of the linear combination of the following restraints: (1) cross-correlation to the EM map (FitRestraint of IMP), (2) connectivity distance between domains neighbouring in sequence, (3) clash score (SoftSpherePairScore of IMP), and (4) a soft restraint favouring approximate twofold symmetry. The structures were simultaneously represented at two resolutions: in Cα-only representation and a coarse-grained representation, in which each ten-residue stretch was converted to a bead. The ten-residue bead representation was used for the clash score and the electron microscopy and symmetry restraint to increase computational efficiency, the Cα-only representation was used for domain connectivity restraints. Five-hundred independent Monte Carlo optimizations were run until convergence and the best scoring model was selected as the final model. The models of the Y-complex fitted into CR and NR could not be obtained by rigid body fitting of the published models[15]. Therefore, we have divided the available crystal structures and homology models[15] into smaller (six for the CR and seven for the NR Y-complex) rigid bodies (with cut points corresponding to boundaries of published crystal structures of Y-subcomplexes) and fitted them simultaneously into the NR and CR segments of the cryo-EM *S. cerevisiae* NPC map from this study using the integrative modelling procedure described previously[55,66] using IMP[65] version develop-54df7231ec. At first, each of the rigid bodies has been independently fitted to the NPC cryo-EM map using UCSF Chimera[60] as described above to generate libraries of alternative non-redundant fits for each rigid body. Then, we generated configurations of all the rigid bodies by recombining the aforementioned fits using simulated annealing Monte Carlo optimization. Each configuration was generated by an independent Monte Carlo optimization comprising 60,000 steps resulting in total 20,000 models and scored. The scoring function for the optimization was a linear combination of the EM fit restraint represented as the *P* values of the precalculated domain fits (from systematic fitting as described above), domain connectivity restraint, a term preventing overlap of the Y components with the nuclear envelope and the assigned Nup159 complex density, and clash score (see ref. [55]. for the implementation details). The structures were simultaneously represented at two coarse-grained resolutions 1 and 10 as above for the refinement of the IR. Since the *P* values were derived from the original EM fits generated with UCSF Chimera, the EM restraint can be regarded as an EM restraint derived from the full atom representation. For the CR, the top scoring model was selected for visualization and proposed as final. For the NR, the final model was additionally refined using the above refinement procedure and additional restraints to anchor membrane-binding domains to the nuclear envelope (see below) and the second best scoring refined model was selected for visualization (the top scoring model exhibited a clearly erroneous displacement of one of the rigid bodies, concerning the Nup84–Nup133 interface, but had similar score and conformation of other rigid bodies).

The maps of the NPCs in the mutant strains were built by first rigidly fitting the Y and IR models of the wild-type NPC and then refining the model using the refinement protocol as for the IR in the wild-type NPC. For the *nup116Δ* 25 °C NPC map, both Y-complexes and all four IR subcomplexes (the complexes of Nup(157–170)–Nup(188–192)–Nic96–Nsp1–Nup57–Nup49) could be fitted at the rigid body fitting step and were used for the refinement. In the case of the *nup116Δ* 37 °C NPC map, only the outer nuclear copy out of the four IR subcomplexes fitted to the IR with a poor fit of the Nsp1–Nup57–Nup49 coiled-coil.

Therefore, only the single copy of Nup157–Nup188–Nic96 was refined and included in the final model. Additional restraints were used that (1) favoured preservation of the WT inter-subunit interactions using an elastic network of harmonic distance restraints between interface beads of interacting domains, (2) penalized overlap of protein mass with the nuclear envelope. Also, no symmetry restraint was used for the knockout maps. For the *nup116Δ* 37 °C NPC map, an additional restraint favouring interactions of the Nup157 β-propeller with the nuclear envelope was used (derived using MapDistanceTransform of IMP).

Supplementary Videos 1, 2, 4 were created with UCSF Chimera[60]. Supplementary Videos 3, 5, 6–10 were prepared with IMOD[49] and Movavi Video Editor 15.

Reporting summary

Further information on research design is available in the Nature Research Reporting Summary linked to this paper.

Data availability

The three cryo-EM maps associated with this manuscript have been deposited in the Electron Microscopy Data Bank under accession numbers EMD-10198, EMD-10660 and EMD-10661. The integrative models of S. cerevisiae NPC are available at Zenodo at https://doi.org/10.5281/zenodo.3820319 and the PDB-Dev database under accession numbers PDBDEV_00000051, PDBDEV_00000052 and PDBDEV_00000053. Unprocessed western blots are available in Supplementary Fig. 1. Because of their size, original imaging data are available from the corresponding author upon request.

Code availability

The input data and the scripts used for modelling are available at Zenodo at https://doi.org/10.5281/zenodo.3820319.

46. Schindelin, J. et al. Fiji: an open-source platform for biological-image analysis. *Nat. Methods* **9**, 676–682 (2012).
47. Hampoelz, B. et al. Pre-assembled nuclear pores insert into the nuclear envelope during early development. *Cell* **166**, 664–678 (2016).
48. Mastronarde, D. N. Automated electron microscope tomography using robust prediction of specimen movements. *J. Struct. Biol.* **152**, 36–51 (2005).
49. Kremer, J. R., Mastronarde, D. N. & McIntosh, J. R. Computer visualization of three-dimensional image data using IMOD. *J. Struct. Biol.* **116**, 71–76 (1996).
50. Paul-Gilloteaux, P. et al. eC-CLEM: flexible multidimensional registration software for correlative microscopies. *Nat. Methods* **14**, 102–103 (2017).
51. de Chaumont, F. et al. Icy: an open bioimage informatics platform for extended reproducible research. *Nat. Methods* **9**, 690–696 (2012).
52. Rigort, A. et al. Focused ion beam micromachining of eukaryotic cells for cryoelectron tomography. *Proc. Natl Acad. Sci. USA* **109**, 4449–4454 (2012).
53. Schaffer, M. et al. Optimized cryo-focused ion beam sample preparation aimed at in situ structural studies of membrane proteins. *J. Struct. Biol.* **197**, 73–82 (2017).
54. Hagen, W. J. H., Wan, W. & Briggs, J. A. G. Implementation of a cryo-electron tomography tilt-scheme optimized for high resolution subtomogram averaging. *J. Struct. Biol.* **197**, 191–198 (2017).
55. Kosinski, J. et al. Molecular architecture of the inner ring scaffold of the human nuclear pore complex. *Science* **352**, 363–365 (2016).
56. Zhang, K. Gctf: Real-time CTF determination and correction. *J. Struct. Biol.* **193**, 1–12 (2016).
57. Turoňová, B., Schur, F. K. M., Wan, W. & Briggs, J. A. G. Efficient 3D-CTF correction for cryo-electron tomography using NovaCTF improves subtomogram averaging resolution to 3.4Å. *J. Struct. Biol.* **199**, 187–195 (2017).
58. Beck, M., Lucić, V., Förster, F., Baumeister, W. & Medalia, O. Snapshots of nuclear pore complexes in action captured by cryo-electron tomography. *Nature* **449**, 611–615 (2007).
59. Kucukelbir, A., Sigworth, F. J. & Tagare, H. D. Quantifying the local resolution of cryo-EM density maps. *Nat. Methods* **11**, 63–65 (2014).
60. Pettersen, E. F. et al. UCSF Chimera—a visualization system for exploratory research and analysis. *J. Comput. Chem.* **25**, 1605–1612 (2004).
61. Wriggers, W. Conventions and workflows for using Situs. *Acta Crystallogr. D* **68**, 344–351 (2012).
62. Strimmer, K. fdrtool: a versatile R package for estimating local and tail area-based false discovery rates. *Bioinformatics* **24**, 1461–1462 (2008).
63. Benjamini, Y. & Hochberg, Y. Controlling the false discovery rate: a practical and powerful approach to multiple testing. *J. R. Stat. Soc. B* **57**, 289–300 (1995).
64. Kosinski, J. et al. Xlink Analyzer: software for analysis and visualization of cross-linking data in the context of three-dimensional structures. *J. Struct. Biol.* **189**, 177–183 (2015).
65. Webb, B. et al. Integrative structure modeling with the Integrative Modeling Platform. *Protein Sci.* **27**, 245–258 (2018).

Article

66. Dauden, M. I. et al. Architecture of the yeast Elongator complex. *EMBO Rep.* **18**, 264–279 (2017).

Author contributions M.A. conceived the project, designed experiments, collected cryo-EM, electron microscopy, CLEM and light microscopy data, analysed data and wrote the manuscript. C.E.Z. designed experiments, collected cryo-EM data, analysed data and wrote the manuscript. V.R. performed integrative modelling, analysed data and wrote the manuscript. F.W. designed experiments, collected light microscopy and functional autophagy data and analysed data. P.R. designed experiments, collected CLEM and electron microscopy data and analysed data. H.K.H.F. collected cryo-confocal data and analysed data. X.Z. collected cryo-confocal data. C.-W.L. collected functional autophagy data and analysed data. M. Börmel collected electron microscopy data. W.H. collected cryo-EM data. B.T. analysed subtomograms. K.K. performed integrative modelling. C.W.M., J.M. and Y.S. supervised the project. B.P., J.K. and M. Beck conceived the project, designed experiments, supervised the project and wrote the manuscript.

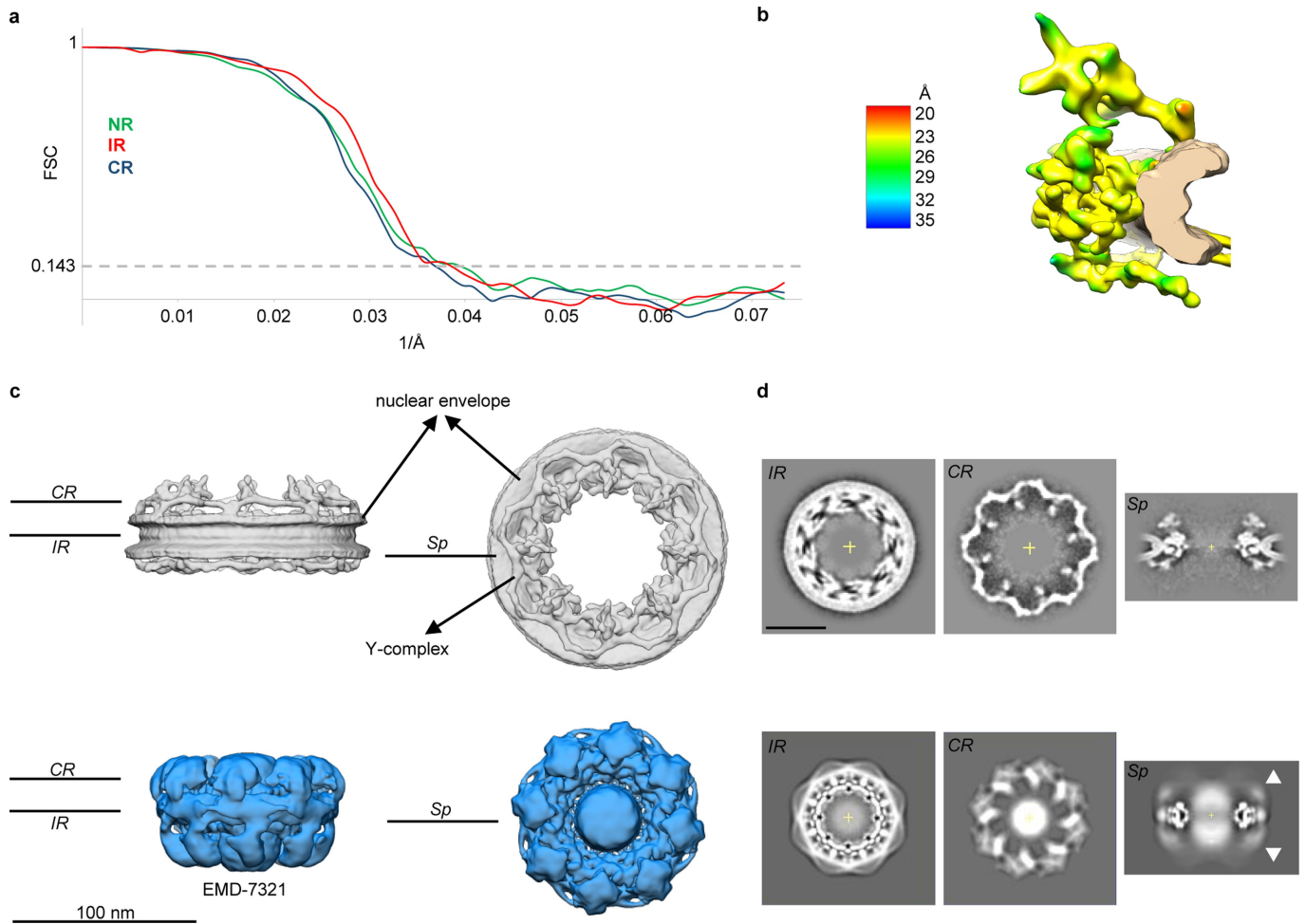**Competing interests** The authors declare no competing interests.

Extended Data Fig. 1 | In-cell structure of the *S. cerevisiae* NPC vs detergent-extracted NPC (EMD-7321). a, Gold standard FSCs of in-cell cryo-EM map of the *S. cerevisiae* NPC. All the curves (nuclear ring NR, cytoplasmic ring CR, inner ring IR) intersect the 0.143 criterium at around 25 Å resolution. **b**, Local resolution analysis[59] with colour-coded bar. **c**, In-cell cryo-EM map (grey, average of *n* = 250 NPCs) in comparison to cryo-EM map of detergent-extracted *S. cerevisiae* NPCs (blue, EMD-7321 at the suggested

contour level) show significant differences in diameter and in interpretable features. The nuclear membranes and the Y-complexes are clearly discerned in the in-cell cryo-EM map, in contrast to EMD-7321. **d**, Tomographic slices through the maps shown in **c** at the level of the cytoplasmic (CR) and inner rings (IR) and an individual spoke (Sp). Lines in **c** indicate slicing position shown in **d**. Arrowheads indicate blurred features in the outer rings. Scale bar: 50 nm.

Article

IR, fitted structure: Yeast IR complex (PDB DEV ID: 00000010)
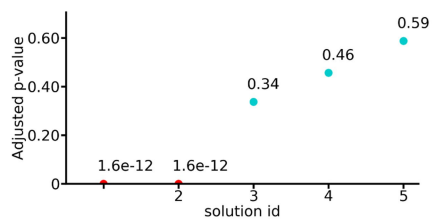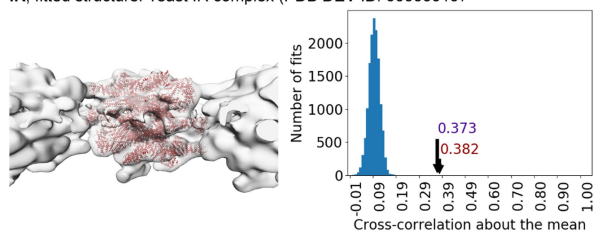
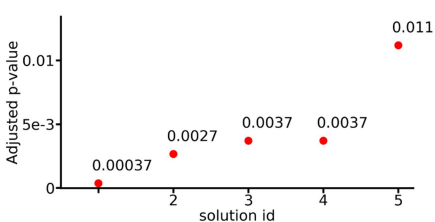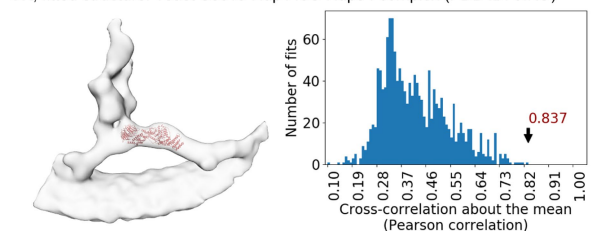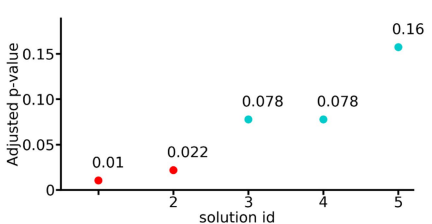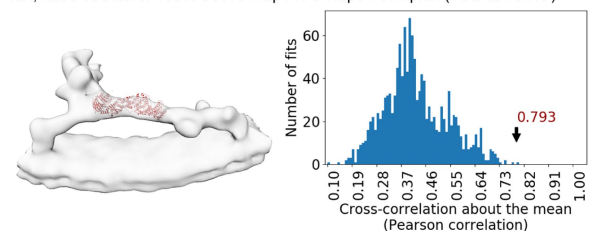**CR**, fitted structure: Yeast Y complex (PDB ID: 4XMM)
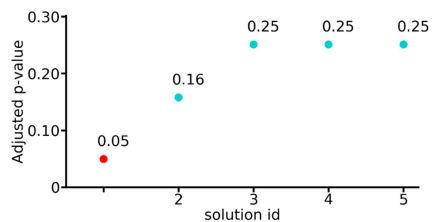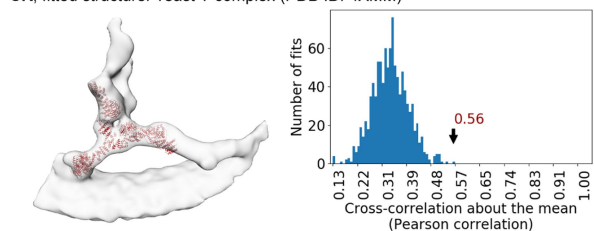
NR, fitted structure: Yeast Y complex (PDB ID: 4XMM)
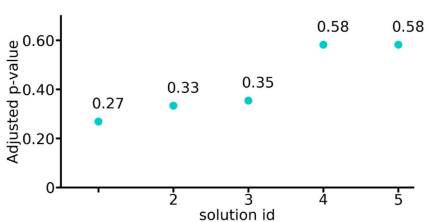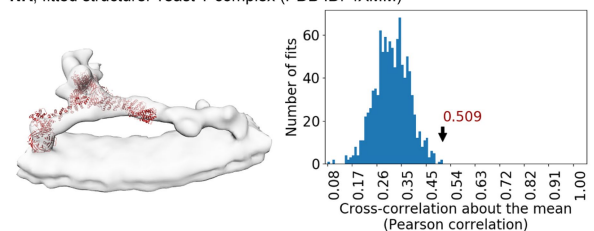
CR, fitted structure: Yeast Sec13-Nup145C-Nup84 complex (PDB ID: 3IKO)

NR, fitted structure: Yeast Sec13-Nup145C-Nup84 complex (PDB ID: 3IKO)

NR, fitted structure: Yeast Nup84-Nup133 complex (homology model, Fernandez-Martinez, 2016)
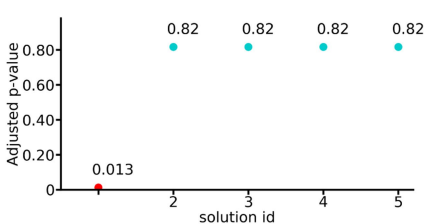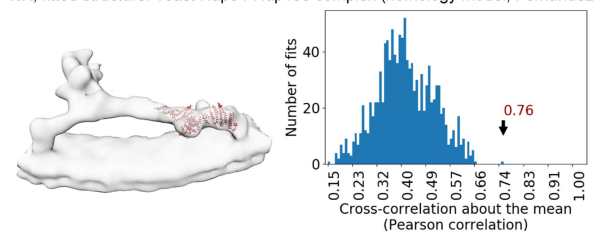
Extended Data Fig. 2 | See next page for caption.

Extended Data Fig. 2 | Systematic fitting of inner and outer ring components into the *S. cerevisiae* NPC map. Each row shows the visualization of the top fits (left), the histogram of raw scores (middle), and a plot of the top five *P* values (right). In the *P* value plots, the statistically significant fits are coloured red (*P* < 0.05; *P* values were calculated using the two-sided test as implemented in fdrtool R-package, see Methods). All *P* values were adjusted for multiple comparisons using Benjamini-Hochberg procedure. The top fits are indicated in the histograms with an arrow and the score value. The number of sampled fits used to calculate *P* values after clustering of similar solutions was 14,348, 1,015, 1,039, 1,479, 1,354, and 1,183 for the rows from top to bottom. For the IR, the integrative model of the single spoke of the IR[15] was used as the fitted structure. For the outer rings (CR and NR), the crystal structure of the yeast Y-complex was fitted or its parts corresponding to subcomplexes. The structures were fitted by an unbiased global search using UCSF Chimera[60] and scored using the cross-correlation score about the mean as explained in the Methods. The IR complex was fitted to the entire spoke map, while the other structures were fitted to individual CR and NR segments.

Article
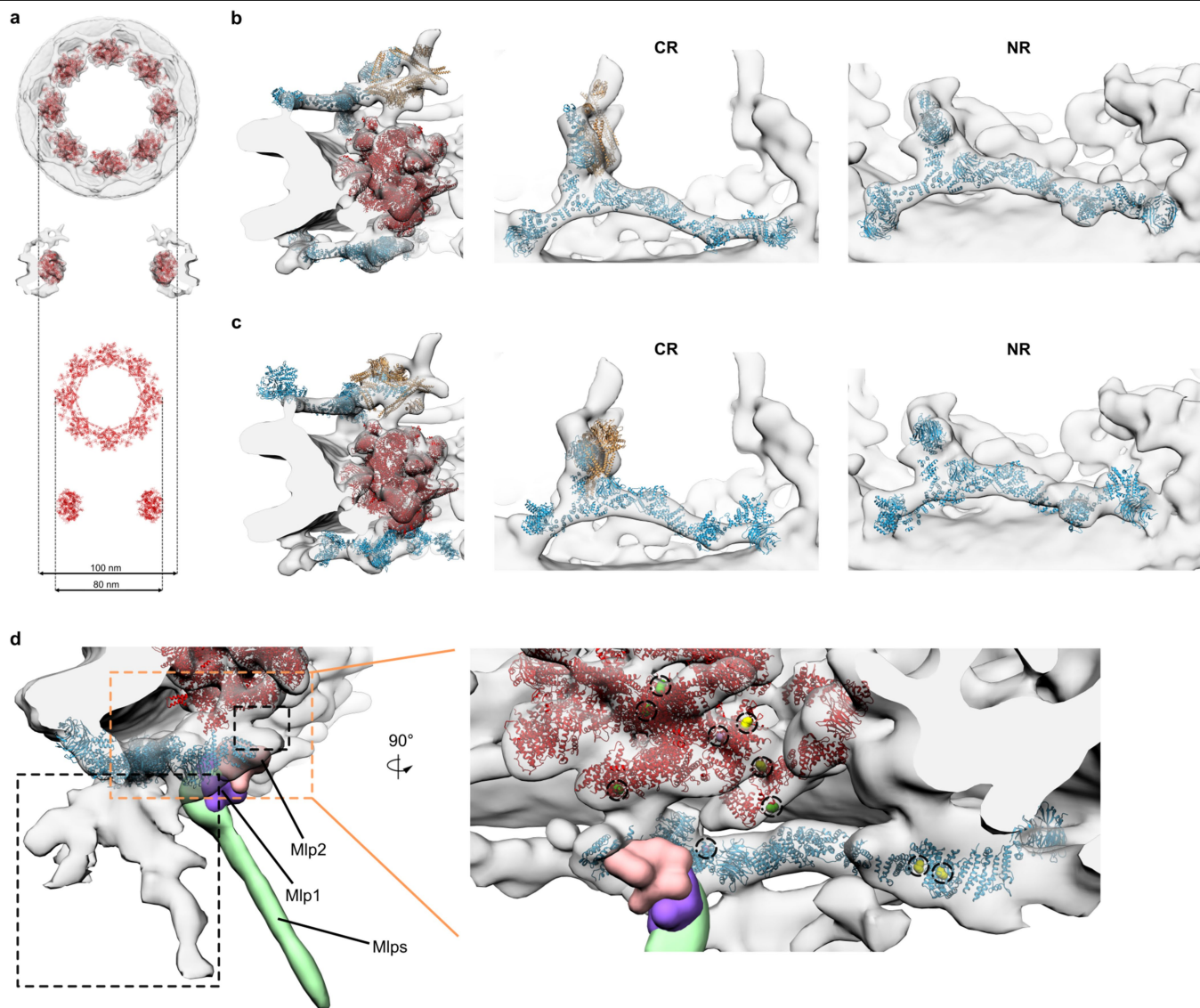
Extended Data Fig. 3 | Architectural model of *S. cerevisiae* NPC.
a, Comparison of fitted (to the *S. cerevisiae* NPC map from this study, depicted in grey) integrative inner ring complex models (red ribbons) from[15] with 20 nm diameter difference. **b**, Representative integrative structural models of CR and NR Y-complex (blue ribbons) built in this work (see Methods) shown with the integrative model of P-complex (yellow ribbons) and refined IR (red ribbons) from[15] fitted to the allocated density of the in-cell map (grey density) from this study. The Y-complexes are more extended as compared to reference[15] version by ~40 Å. **c**, Representative integrative structural models of CR and NR Y-complex (blue ribbons), P-complex (yellow ribbons) and IR (red ribbons) from[15] (PDB-Dev ID: PDBDEV_00000010) fitted to the *S. cerevisiae* NPC map (grey density) from this study, with respect to spatial reference frame from[15]. **d**, Representative integrative structural model of NR Y-complex (blue ribbons) built in this work shown together with the integrative model of the refined IR (red ribbons) from[15] fitted to the allocated density of the *S. cerevisiae* NPC map (grey density). The localization probability densities of Mlp1, Mlp2 and Mlp1/

Mlp2 ensemble from[15] are displayed in orientation relative to the NR Y-complex as in[15]. Local mask refinement of *n* = 250 NPCs recovers extra densities in the NR that locate around the Nup120-Nup145C junction and the Nup107-Nup133 stem (left dark dotted frame). Most likely these densities account for parts of the basket since it resembles a filamentous structure[15]. It anchors to the regions of the Y-complex that crosslink to Mlp1 or Mlp2[15] and connects to the Nup85-Seh1 arm as proposed by the previous model[15], but contrary to[15], the filamentous region centres at the Y-complex vertex rather than at the Nup85 arm. On the right panel residues crosslinking to Mlp1 or Mlp2[15] are shown in sphere representation and coloured according to their confidence score (from[15]) with yellow – *P* < 0.01, green – *P* < 0.1, magenta *P* > 0.1. The shown residues, together with the yet unmodelled crosslink to residue 2 of Nup85[15], emphasize that the highest confidence crosslinks are associated to the Y-complex, while the lowest confidence ones are associated to the IR. A second density (right dark dotted frame) remains unassigned, being proximate to residues crosslinking with Nup116, Nup100, Nup145N (see Extended Data Fig. 5c).

a

CR, fitted structure (using UCSF Chimera): Negative stain map of the Yeast Nup159 complex (Gaik et al., 2015)

CR, fitted structure (using UCSF Chimera): Negative stain map of the Yeast Nup159 complex **mirror image**

CR, fitted structure (using Situs colores): Negative stain map of the ScNup159 complex (Gaik et al., 2015)

b

Nup159 DID/Dyn2

Nup159 complex (Kim et al, 2018)

FG-repeats

Nup159 complex (Kim et al, 2018) positioning by this study

Nup82 ß-propellers

Nup82 ß-propellers

180°

FG-repeats

Nup159 DID/Dyn2

c

Nup159 complex (Kim et al, 2018) positioning by this study

Nup116 (PDB ID: 3pbp)

d

ScNup82-ScNup159-ScNup116 complex (PDB ID: 3pbp)

e

Nup159 complex (Kim et al, 2018) positioning by this study

Nup159 complex - Y complex crosslinks

Y (new model)

Cryo-ET map

Nup159 complex (Kim et al, 2018)

Nup159 complex - Y complex crosslinks

Y (Kim et al, 2018)

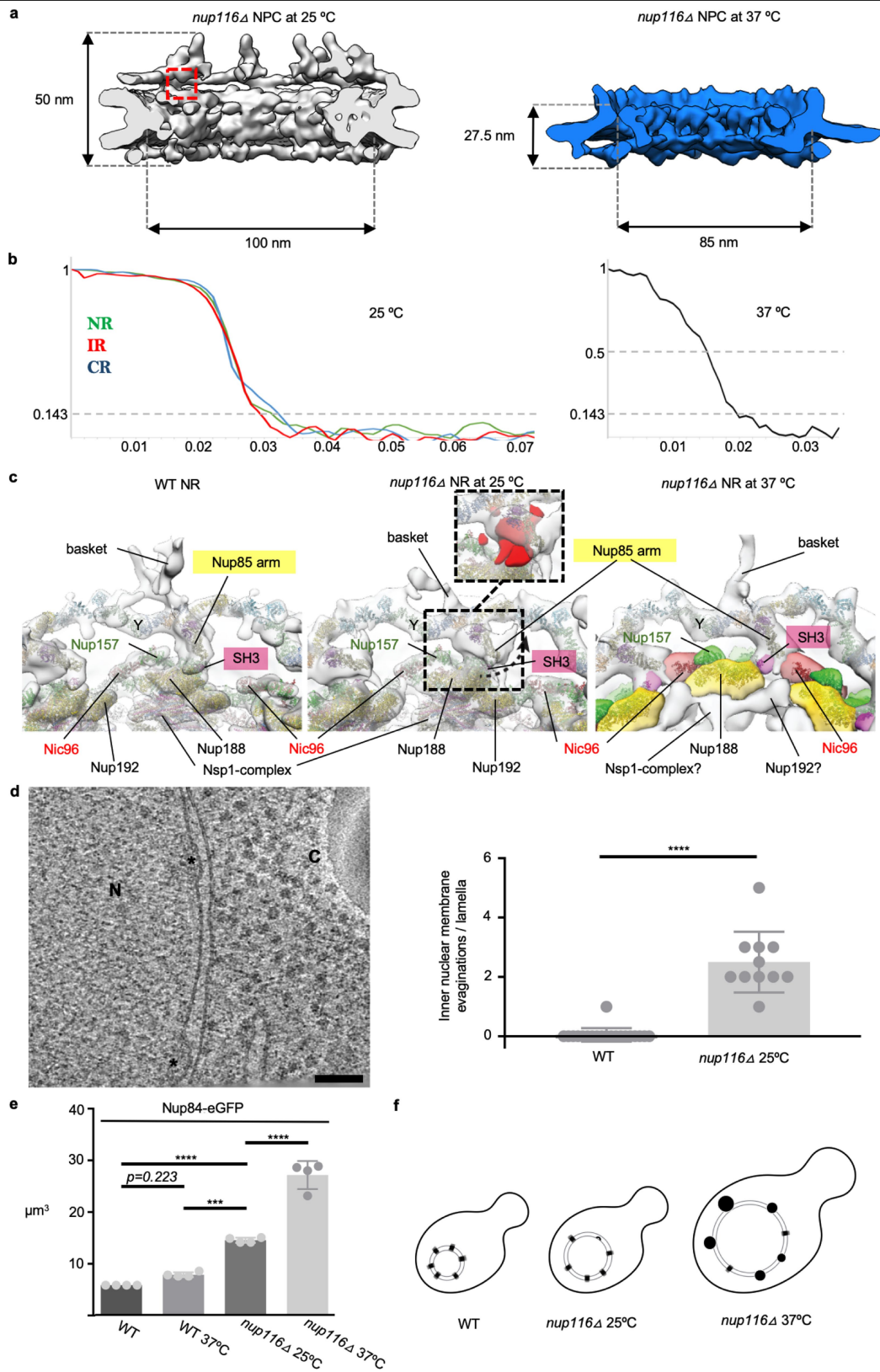**Extended Data Fig. 4** | See next page for caption.

Article

Extended Data Fig. 4 | Validation of the orientation of the Nup159 complex.
a, Systematic fitting of the negative stain map of the Nup159 complex (yellow) into the *S. cerevisiae* NPC map (grey) using UCSF Chimera[60] and Colores program from the Situs package[61]. As a negative control, also the mirror image of the negative stain map was fitted but did not lead to significant scores, further underlining the unambiguous nature of the fits. Each row shows the visualization of the top fits (left), the histogram of raw scores (middle), and a plot of the top five *P* values (right). In the *P* value plots, the statistically significant fits are coloured red (*P* < 0.05; *P* values were calculated using the two-sided test as implemented in fdrtool R-package, see Methods). All *P* values were adjusted for multiple comparisons using Benjamini-Hochberg procedure. The top fits are indicated in the histograms with an arrow and the score value. The number of sampled fits used to calculate *P* values after clustering of similar solutions was 585, 599, and 2243, for top, middle, and bottom rows respectively. **b**, Representative integrative Nup159 complex model from[15] inside the in-cell *S. cerevisiae* NPC map (grey mesh) in the orientation determined in this work (left) versus the previously published orientation (right). The Nup159 complex model is shown in orange ribbons within yellow localization probability density from[15] locally fitted with UCSF Chimera[60]. The previous orientation was reproduced by first fitting the entire model from[15] to the in-cell cryo-EM map and then locally fitting the Nup159 complex to the density (which was needed to bring the Nup159 complex into the density and preserve the orientation). The dashed grey line indicates the flipping axis between the two fits. **c**, Superimposition of the crystal structure 3PBP[27] onto the Nup82 β-propellers from the representative integrative Nup159 complex model from[15] in the revised orientation predicts the position of Nup116, as confirmed by our knockout study (Fig. 2c). **d**, Visualization of two of the top resulting systematic fits of the 3PBP crystal structure into the cryo-ET map presented in this study confirms our *nup116Δ* structure (Fig. 2c). **e**, Crosslinks between the Nup159 complex and the Y-complex from[15] support the new orientation (left) compared to the published orientation (right). Satisfied and violated crosslinks are depicted as blue and red bars respectively while the Nup159 complex and the Y-complex from[15] are depicted within the relevant localization probability densities from[15].

a

Y
new model

Nup159
complex
(Kim et al, 2018)
positioning by
this study

Nup116 CTD
positioning by
this study

Nup116
connector cable
(Kim et al, 2018)

IR
(Kim et al, 2018)

Y
new model

Nup159
complex
(Kim et al, 2018)
positioning by
this study

Nup116 CTD
positioning by
this study

Nup116
connector cable
(Kim et al, 2018)

IR
(Kim et al, 2018)

Y
new model

Cryo-ET map

b

Nup116 CTD

Nup159
complex

Nup116
connector cable

IR

Nup116 CTD

Nup159
complex

Nup116
connector
cable

IR

Y

Y

**Localization
probability densities**
with representative atomic model

c

CR

Cryo-ET map

NR

Nup145N

Nup116

Nup116

SH3-like
domain

Nup116(2)   Nup116   Nup116(2)   Nup116(2)
                          Nup100   Nup100
                                       Nup145N

Nup116(2)
Nup100
Nup145N

SH3-like
domain

Nup145N

Nup116

Nup116   Nup116(2)   Nup116(2)   Nup116
           Nup100

Extended Data Fig. 5 | See next page for caption.

Article

Extended Data Fig. 5 | Nup116 positioning and possible Nup188 SH3-like domain interactions. a, New positioning of the Nup116 versus **b**, previously published integrative model (PDB-Dev ID: PDBDEV_00000010 from[15], right). The two *S. cerevisiae* NPC models were superimposed such that the IRs are aligned to the same reference frame. The Nup116 position is shown either as the density assigned to Nup116 based on the Nup116 knockout structure in the CR (**a**) or as localization probability densities retrieved from reference[15] model (**b**). The major structural elements of the NPC are indicated. The Nup116 connector cable in the in-cell model (**a**) has been taken from reference[15] based on its position relatively to the IR. Blue bars represent crosslinks from Nup116 to other Nups[15]. For the in-cell model, the cryo-ET map is displayed; for the model from[15], the localization probability densities (not an EM map) are shown instead. **c**, SH3-like domain (magenta ribbons and dotted frames) of Nup188[28] (yellow ribbons) bridges the interactions between the inner and the outer rings. The positions of Nup188 crosslinking to Nup116 (the number of times that some Nup188 residues crosslink with more than one Nup116 residues are denoted in the labels in parenthesis), Nup100 and Nup145N are indicated in sphere representation (red spheres) and their location suggests that they link the connecting interfaces between the IR and the outer rings: NR brown dotted frame corresponds to an unassigned density, CR green dotted frame corresponds to Nup116 density, NR green dotted frame corresponds to a second Nup116 density, see Extended Data Fig. 6c.

a

nup116Δ NPC at 25 ºC

50 nm

100 nm

nup116Δ NPC at 37 ºC

27.5 nm

85 nm

b

NR
IR
CR

25 ºC

37 ºC

c

WT NR

nup116Δ NR at 25 ºC

nup116Δ NR at 37 ºC

basket   Nup85 arm

Y

Nup157   SH3

Nic96   Nup188   Nup192
Nsp1-complex

basket   Nup85 arm

Y

Nup157   SH3

Nic96   Nup188   Nup192
Nsp1-complex

basket

Nup85 arm   SH3

Y

Nup157

Nic96   Nup188   Nic96
Nsp1-complex?   Nup192?

d

N   *   C

*

Inner nuclear membrane evaginations / lamella

****

WT   *nup116Δ* 25ºC

e

Nup84-eGFP

μm³

****
p=0.223
***
****

WT   WT 37ºC   *nup116Δ* 25ºC   *nup116Δ* 37ºC

f

WT   *nup116Δ* 25ºC   *nup116Δ* 37ºC

Extended Data Fig. 6 | See next page for caption.

Article

Extended Data Fig. 6 | *nup116Δ* NPC structure and nuclear envelope remodelling. a, In-cell structure of *nup116Δ* NPC cut in half along the central axis, at 25 °C on the left and at 37 °C on the right. At 25 °C diameter and general dimensions are alike the WT structure of Fig. 1b. The red dashed square indicates the position of the missing densities at neck region corresponding to Nup116 (see also Fig. 2c and Extended Data Fig. 5a). **b**, FSCs of *nup116Δ* NPC at 25 °C after masking the three rings (NR, IR, CR respectively nuclear, inner and cytoplasmic ring). The curves intersect 0.143 at around 35 Å resolution. On the right FSC of *nup116Δ* NPC at 37 °C calculated with a mask enclosing both the IR and the NR. The average was performed with a pixel size of 13.8 Å (original pixel size 4 times binned). The resolution is ~50 Å. **c**, Structural differences in the NR of the *S. cerevisiae* NPC from WT (left), and *nup116Δ* cells at the permissive (25 °C, middle) and non-permissive (37 °C, right) temperatures. The grey envelope represents the overlay of EM maps generated with two different masks – one enclosing the entire NR and IR and the second centred at the region of the extra densities around the Y-complex. The regions of the major differences are indicated with dashed frames. A shift of the Nup85 arm away from the IR is indicated with a black dashed arrow. The difference density around the Nup85 arm between the NPC maps from *nup116Δ* 25 °C and WT cells is shown in the inset in red and indicates a putative nuclear copy of Nup116 and the conformational shift of the Nup85 arm. Due to the low resolution, the IR of the *nup116Δ* 37 °C is shown as segmented densities assigned based on the fitting of the outer nuclear copy of the IR subcomplex. Question marks indicate predicted assignments based on similarity to the WT map but with a poor density insufficient for fitting. The HideDust tool of UCSF Chimera[60] was used for clarity. **d**, Cryo-tomographic slice of nuclear envelope with inner nuclear membrane evaginations marked with asterisks in *nup116Δ* NPC at 25 °C. The histograms show that the number of inner nuclear membrane evaginations is significantly higher in the nuclear envelope of the mutant cells (32 in $n = 145$ cryo-tomograms, 42 lamellae) in comparison to WT envelopes (1 in $n = 240$ cryo tomograms, 100 lamellae); centre values represent the mean and error bars the SD; $P < 0.0001$ (Mann–Whitney test, two-tailed); N marks the nucleus and C marks cytoplasm, scale bar: 100 nm. **e**, Box plot showing the increase in nuclear size in *nup116Δ* cells in comparison to WT cells (~2.5-fold increase in volume) and a 4 to fivefold increase in comparison to WT upon shift to 37 °C. Light microscopy data of Nup84-eGFP, shown in Fig. 3c, were used to quantify the difference in nuclear volume as explained in the methods section. $n = 100$ nuclei were measured for each strain from four independent biological replicates (filled circles represent averages of the independent biological replicates). The statistical significance was evaluated with by one-way ANOVA with Dunn's multiple comparisons test; centre values represent the mean and error bars the SD; ***$P < 0.0002$, ****$P < 0.0001$). **f**, Cartoon model depicting the summary of the results coming from Fig. 3c, d, e and Extended Data Fig. 6d, e. NPC are represented as black cylinders, NPC-concealing herniae as black circles, a nuclear membrane evagination is shown as semicircle.
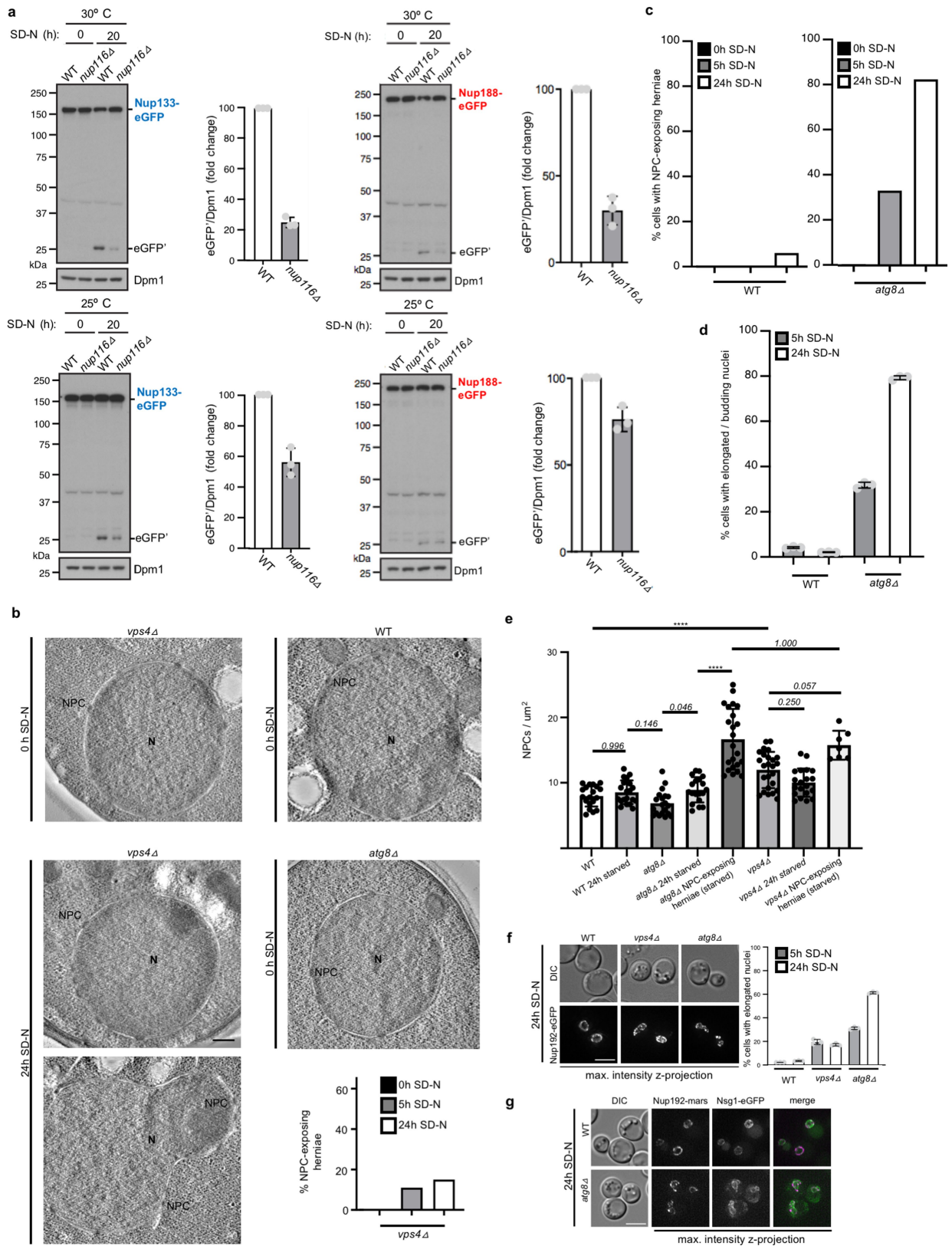
Extended Data Fig. 7 | See next page for caption.

Article

Extended Data Fig. 7 | NPC degradation and nuclear envelope reshaping upon starvation. a, western blot and quantification of the degradation of Nup133, Nup188 upon Nitrogen starvation at 25 °C and 30 °C in WT and *nup116Δ* strain. eGFP was measured using anti-eGPF immunoblotting. eGFP' denotes vacuolar eGFP remnant. Dpm1 was used as a loading control. Centre values represent the mean and error bars the s.d. of $n = 3$ biologically independent replicates. At 30 °C, Nup133, Nup188 are degraded fourfold less in comparison to WT. **b**, Typical tomographic plastic section of WT, *atg8Δ S. cerevisiae* nuclei after 0h of starvation (negative control of Fig. 4c) or of *vps4Δ S. cerevisiae* nuclei after 0 or 24 h of starvation. Quantification of number of NPC-exposing herniae at 0, 5 and 24 h of starvation is shown for *vps4Δ* cells. We show an example of a round nucleus and of an NPC-exposing hernia from those cells. $n = 85$ tomograms of nuclei for WT; $n = 84$ for *vps4Δ*; $n = 83$ for *atg8Δ*; $n = 62$ for *vps4Δ* 24h starved; $n = 64$ for *vps4Δ* 5h starved; see Supplementary Table 2. N marks the nucleus. Scale bar, 200 nm. **c**, Quantification of of NPC-exposing herniae from plastic section tomograms as in Fig. 4c at 5h and 24h of starvation. After 24h, 82% of nuclei in the *atg8Δ* cells contain NPC-exposing herniae ($n = 78$ tomograms in average for each condition, see Supplementary Table 2).

d, Quantification of deconvoluted wide-field maximum intensity projection images as in Fig. 4d from three biologically independent replicates and $n = 300$ per replica. **e**, Quantification of NPC density (NPCs/µm²) from plastic sections tomograms as in **c** shows clustering of NPCs in NPCs-exposing hernia. The statistical significance was evaluated with one-way ANOVA with Dunn's multiple comparisons test ($n = 20$ tomograms per strain except *vps4Δ* NPC-exposing herniae where $n = 5$ tomograms; the average nuclear envelope surface measured per strain is 20 µm², except *atg8Δ* NPC-exposing herniae where is 11 µm² and *vps4Δ* NPC-exposing herniae where is 3.5 µm²; ****$P < 0.0001$; centre values represent the mean and error bars the SD). **f**, Phase contrast and deconvoluted wide-field max intensity projection of WT, *vps4Δ* and *atg8Δ* cells imaged live before and after 24h of starvation with eGFP-tagged Nup192 as marker. The quantification is derived from three independent biological replicates where five images with at least $n = 250$ nuclei per replicate; central bars represent the mean and error bars the s.d. The trend of nucleus deformation is the same seen in **b**. **g**, Same as **c** for WT and *atg8Δ* cells, but with the inner nuclear membrane marker Nsg1. Data are derived from three independent biological replicates with at least $n = 250$ nuclei per replicate.

a

p<0.00001

b
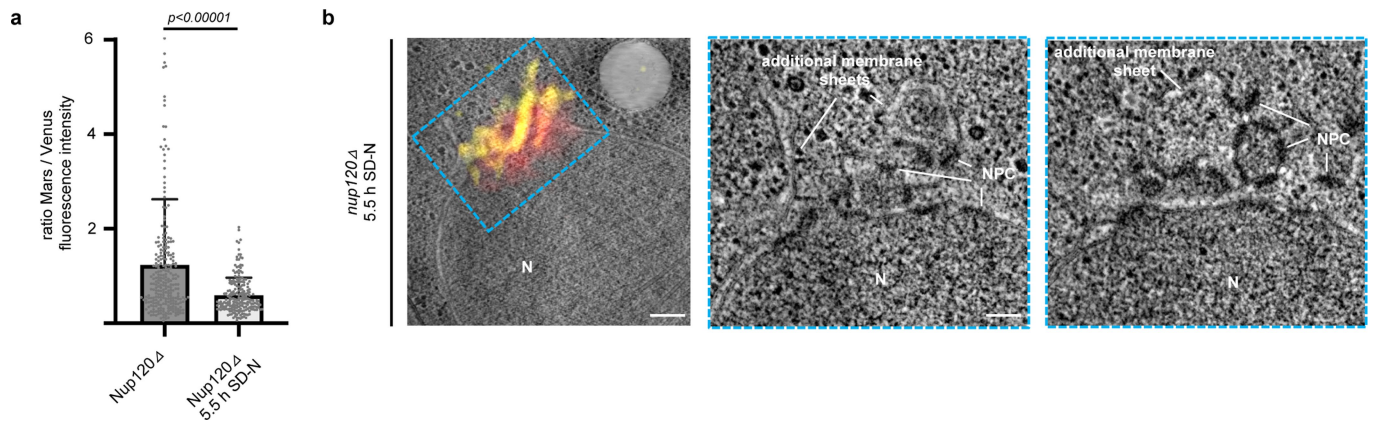
nup120Δ
5.5 h SD-N

Extended Data Fig. 8 | Interaction Nup159-Atg8 upon starvation.
a, Fluorescence intensity analysis of *nup120Δ*, Nup170-Mars, Nup159-Atg8-split Venus nuclei spots before and after 5.5 h of starvation. The ratio Mars/Venus shows the significant increase in Venus signal as compared to Mars signal in this starved strain. Three biological replicates and *n* = 100 spots per replicate were measured (*P* < 0.00001, Mann–Whitney, two-sided; box centres represent the mean and error bars the s.d.). **b**, Tomographic slice (plastic section) overlaid with wide-field fluorescent image obtained by on section-CLEM[37,45] of the strain in **a** upon ~6 h of starvation. *n* = 36 correlated tomograms (technical replicates) were acquired and 24 (75%) had similar results. 8 spots come from uranyl autofluorescence in the cytoplasm. Venus signal is shown in yellow. Nup170-Mars is shown in red. The cyan dashed rectangle indicates the area zoomed into the two right panels showing tomographic slices at two different Z-heights (N marks the nucleus, scale bar: 200 nm). See also Supplementary Videos 9, 10.
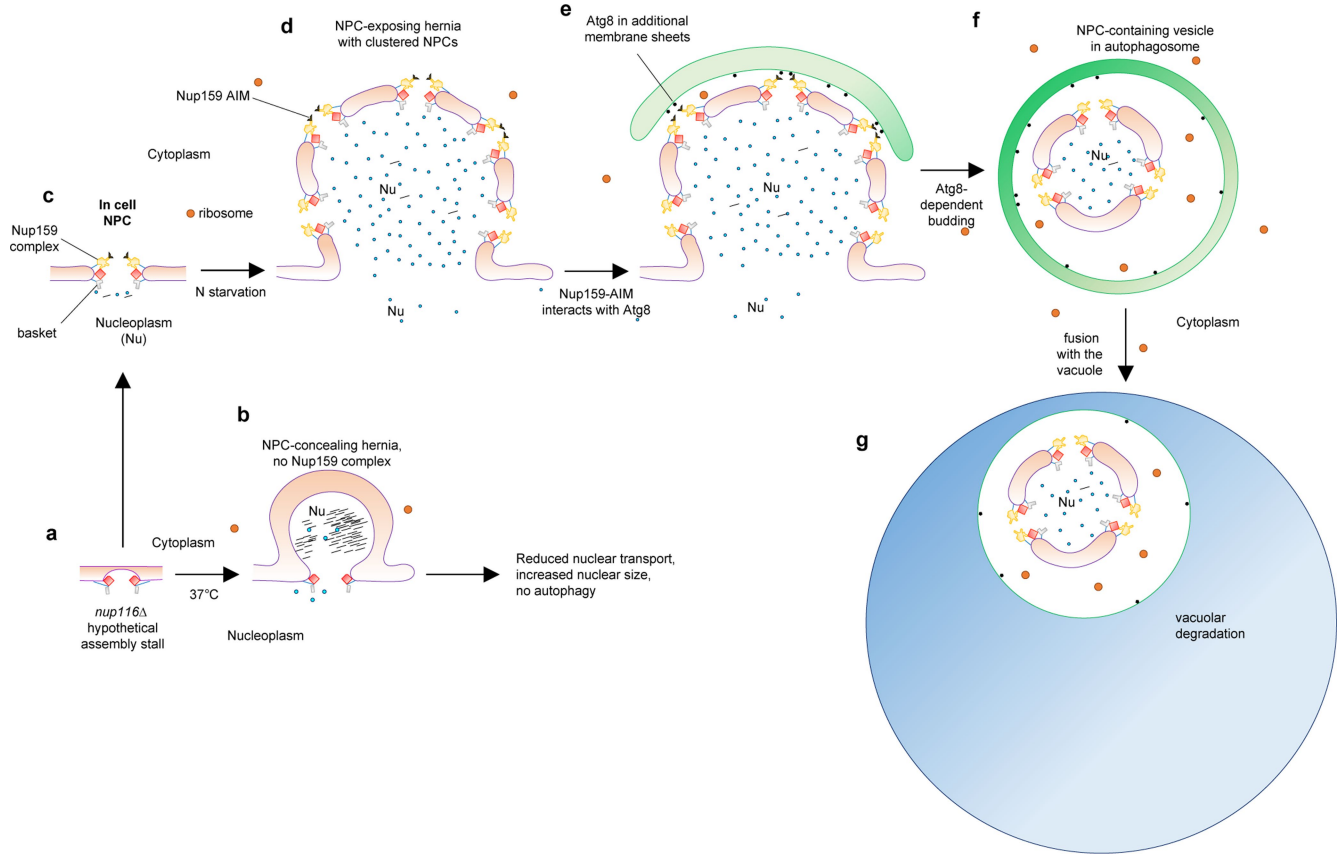
Extended Data Fig. 9 | Model of membrane remodelling in NPC-concealing and NPC-exposing hernia. a, Plausible inside-out assembly intermediate[33] or inner nuclear membrane evaginations (Extended Data Fig. 6d) progress into **b**, NPC-concealing herniae (Fig. 3a, Supplementary Video 3) which accumulate over time (Fig. 3d), concomitantly with increasing nuclear size (Extended Data Fig. 6e;[3]). Black lines indicate dark material present in cryo tomograms, possibly poly-A mRNA[3]. **a** matures into **c**, fully assembled NPCs as structurally analysed in cells frozen in exponential growth phase (Fig. 1b, c, Extended Fig. 3d). **d**, When autophagy is triggered by nitrogen starvation, NPCs cluster at the NPC-exposing hernia as in *atg8Δ* (Fig. 4c, d, Extended Data Fig. 7c–e, Supplementary Video 6). **e**, NPC clustering allows high avidity between Atg8 and Nup159 (Fig. 4b, Extended Data Figs. 7e, 8a, b, Supplementary Videos 5, 8, 9, 10) causing nuclear envelope budding depicted in **f**. **f**, Autophagosomes harbouring NPC-containing nuclear vesicles (Fig. 4e, Supplementary Video 7) are transported through the cytosol for degradation in the vacuole (**g** as in Fig. 4f). Colour-code as in Fig. 4e except that nuclear envelope membranes are depicted pink. Ribosomes are depicted as red circles; nuclear material as blue circles.

Extended Data Table 1 | Cryo-EM data collection, refinement and validation statistics

	#1 *Sc*NPC WT (EMDB-10198)	#2 *Sc*NPC nup116Δ 25°C (EMDB-10660)	#3 *Sc*NPC nup116Δ 37°C (EMDB-10661)
Data collection and processing			
Magnification	42.000x	42.000x	42.000x
Voltage (kV)	300	300	300
Electron exposure (e–/Å^2)	~140	~140	~140
Defocus range (μm)	-2 to -4.5	-2 to -4.5	-2 to -4.5
Pixel size (Å)	3.37	3.37	3.37
Symmetry imposed	C8 / C1	C8 / C1	C8 / C1
Initial particle images (no.)	~500 NPCs / ~4000 AU	~250 NPCs/ ~2000 AU	~60 NPCs/ ~480 AU
Final particle images (no.)	~2000 AU	~1300 AU	~450 AU
Map resolution (Å)	25	35	50
FSC threshold	0.143	0.143	0.143
Map resolution range (Å)	20-30	-	-

Corresponding author(s): Martin Beck, Jan Kosinski, Boris Pfander

Last updated by author(s): May 11, 2020

Reporting Summary

Nature Research wishes to improve the reproducibility of the work that we publish. This form provides structure for consistency and transparency in reporting. For further information on Nature Research policies, see Authors & Referees and the Editorial Policy Checklist .

Statistics

For all statistical analyses, confirm that the following items are present in the figure legend, table legend, main text, or Methods section.

n/a	Confirmed	
☐	☒	The exact sample size (n) for each experimental group/condition, given as a discrete number and unit of measurement
☐	☒	A statement on whether measurements were taken from distinct samples or whether the same sample was measured repeatedly
☐	☒	The statistical test(s) used AND whether they are one- or two-sided *Only common tests should be described solely by name; describe more complex techniques in the Methods section.*
☒	☐	A description of all covariates tested
☐	☒	A description of any assumptions or corrections, such as tests of normality and adjustment for multiple comparisons
☐	☒	A full description of the statistical parameters including central tendency (e.g. means) or other basic estimates (e.g. regression coefficient) AND variation (e.g. standard deviation) or associated estimates of uncertainty (e.g. confidence intervals)
☐	☒	For null hypothesis testing, the test statistic (e.g. F, t, r) with confidence intervals, effect sizes, degrees of freedom and P value noted *Give P values as exact values whenever suitable.*
☒	☐	For Bayesian analysis, information on the choice of priors and Markov chain Monte Carlo settings
☒	☐	For hierarchical and complex designs, identification of the appropriate level for tests and full reporting of outcomes
☒	☐	Estimates of effect sizes (e.g. Cohen's d, Pearson's r), indicating how they were calculated

Our web collection on statistics for biologists contains articles on many of the points above.

Software and code

Policy information about availability of computer code

Data collection	Used software are described in the methods. Serial EM is an open source software regularly updated
Data analysis	Used software are described in the methods. Fiji, IMOD (regurarly updated), SoftWoRx (regularly updated) ICY 2.0.0.0, NovaCTF, Gctf 1.06, 3DCT, UCSF Chimera 1.13 are open source. Graph Pad Prism is a commercially available software available at https://www.graphpad.com/scientific-software/prism/. MATLAB is a commercial software available at https://www.mathworks.com/downloads/. Movavi Video Editor 15 is a commercially available software at https://www.movavi.com/mac-video-editor/. The input data and the scripts used for modeling are available at Zenodo (https://zenodo.org/) under the DOI: 10.5281/zenodo.3820319.

For manuscripts utilizing custom algorithms or software that are central to the research but not yet described in published literature, software must be made available to editors/reviewers. We strongly encourage code deposition in a community repository (e.g. GitHub). See the Nature Research guidelines for submitting code & software for further information.

Data

Policy information about availability of data

All manuscripts must include a data availability statement. This statement should provide the following information, where applicable:

- Accession codes, unique identifiers, or web links for publicly available datasets
- A list of figures that have associated raw data
- A description of any restrictions on data availability

The three EM maps associated with this manuscript have been deposited in the Electron Microscopy Data Bank (EMD-10198, EMD-10660, EMD-10661). The integrative models of ScNPC are available at Zenodo (https://zenodo.org/) under the DOI: 10.5281/zenodo.3820319.

Field-specific reporting

Please select the one below that is the best fit for your research. If you are not sure, read the appropriate sections before making your selection.

[✗] Life sciences　　　　[ ] Behavioural & social sciences　　　　[ ] Ecological, evolutionary & environmental sciences

For a reference copy of the document with all sections, see nature.com/documents/nr-reporting-summary-flat.pdf

Life sciences study design

All studies must disclose on these points even when the disclosure is negative.

Sample size	Sample size were chosen from to the practical limitation of the methodology used it was sufficient to interpret the data in a robust way according to standard statistical tests like ANOVA or Mann-Whitney and to previous publications
Data exclusions	No data was excluded from the analyses
Replication	A minimum of three biological replicates were performed for the light microscopy and western blot experiments. Electron microscopy data comes from EM grids prepared in different days from different cell cultures (biological replicates). All attempts of replication were successful
Randomization	All light microscopy and electron microscopy data comes from randomly selected cells
Blinding	Blinding is not relevant for this study because cells are randomly distributed

Reporting for specific materials, systems and methods

We require information from authors about some types of materials, experimental systems and methods used in many studies. Here, indicate whether each material, system or method listed is relevant to your study. If you are not sure if a list item applies to your research, read the appropriate section before selecting a response.

Materials & experimental systems

n/a	Involved in the study
[ ]	[✗] Antibodies
[ ]	[✗] Eukaryotic cell lines
[✗]	[ ] Palaeontology
[✗]	[ ] Animals and other organisms
[✗]	[ ] Human research participants
[✗]	[ ] Clinical data

Methods

n/a	Involved in the study
[✗]	[ ] ChIP-seq
[✗]	[ ] Flow cytometry
[✗]	[ ] MRI-based neuroimaging

Antibodies

Antibodies used	Monoclonal antibody against Dpm1 (1:10,000; clone 5C5A7) was purchased from Invitrogen (Catalog # A-6429) EGFP (1:500; clone B-2) was purchased from Santa Cruz Biotechnology
Validation	The antibodies used in this study were used and validated in previous studies of S. cerevisiae (DOI:10.1038/s41556-019-0459-2). The antibodies are against GFP (clone B-2, Santa Cruz, https://www.scbt.com/p/gfp-antibody-b-2) and against Dpm1 (clone 5C5A7, Invitrogen, https://www.thermofisher.com/antibody/product/DPM1-Antibody-clone-5C5A7-Monoclonal/A-6429).

Eukaryotic cell lines

Policy information about cell lines

Cell line source(s)	Mating_type / Strain_Name / Genotype / Created 1) alpha,WT MATα, his3-Δ200, leu2-3,2-112, lys2-801, trp1-1(am), ura3-52 Fig. 1, 2; Extended Data Fig.1-4 2)a WT MATa his3-Δ200, leu2-3,2-112, lys2-801, trp1-1(am), ura3-52 Fig. 4c, Extended Data Fig.7b 3)alpha Split-Venus-Nup159-Atg8 nup120Δ MATα his3-Δ200, leu2-3,2-112, lys2-801, trp1-1(am), ura3-52 Nup159-VC::HIS3MX6, natNT2::ADH::VN-Atg8, Nup170::mars::kanMX4, nup120Δ::hphNT1 Lee et al, 2020 Fig. 4b, Extended Data Fig. 8b 4) alpha Split-Venus-Nup159-Atg8 MATα his3-Δ200, leu2-3,2-112, lys2-801, trp1-1(am), ura3-52 Nup159-VC::HIS3MX6, natNT2::ADH::VN-Atg8, Nup170::mars::kanMX4 Lee et al, 2020 Revisions 5) a nup116Δ MAT a nup116::HIS3 ade2 his3 leu2 trp1 ura3 kind gift by Hurt lab Fig. 2, 3; Extended Data Fig. 5, 6 6) a atg15Δ Nup192p-yeGFP Nup159p-mars MATa atg15::HIS3MX6 NUP192GFP::kanMX6 NUP159mars::natNT2 or atg15Δ Nup192p-TagGFP Nup159p-mars, his3-Δ200, leu2-3,2-112, lys2-801, trp1-1(am), ura3-52 Lee et al, 2020 Fig. 4e, f

7) alpha nup116Δ Nup188p-yeGFP nup116::natNT2 NUP188GFP::klTRP1 This study Fig. 3f

8) alpha Nup188p-yeGFP NUP188GFP::klTRP1 This study Fig. 3f

9) a nup116Δ Nup133p-yeGFP nup116::natNT2 NUP133GFP::klTRP1 This study Extended Data Fig. 7a

10) alpha Nup133p-yeGFP NUP133GFP::klTRP1 This study Extended Data Fig. 7a

11) alpha Nup120p-yeGFP NUP120GFP::klTRP1 This study Fig. 4d

12) alpha atg8Δ atg8::KAN kind gift by Lusk lab Fig. 4c, Extended Data Fig. 7b

13) alpha atg8Δ Nup120p-yeGFP atg8::kanMX6 NUP120GFP::klTRP1 This study Fig. 4d

14) alpha atg8Δ Nup192p-mars Nsg1p-yeGFP atg8::kanMX6 NUP192Mars::natNT2 NSG1GFP::HIS3MX6 This study Extended Data Fig. 7d

15) alpha Nup192p-mars Nsg1p-yeGFP NUP192Mars::natNT2 NSG1GFP::HIS3MX6 This study Extended Data Fig. 7d

16) alpha vps4Δ vps4::HYG kind gift by Lusk lab Extended Data Fig.7b

17) alpha vps4Δ Nup192p-yeGFP vps4::natNT2 NUP192GFP::klTRP1 This study Extended Data Fig. 7c

18) alpha atg8Δ Nup192p-yeGFP atg8::kanMX6 NUP192GFP::klTRP1 This study Extended Data Fig. 7c

19) alpha Nup192p-yeGFP NUP192GFP::klTRP1 This study Extended Data Fig. 7c

20) alpha Nup84p-yeGFP Nup159p-mars NUP84GFP::klTRP1 NUP159mars::hphNT1 This study Fig. 3c, Extended Data Fig. 6e

21) a nup116Δ Nup84p-yeGFP Nup159p-mars nup116::natNT2 NUP84GFP::klTRP1 NUP159mars::hphNT1 This study Fig. 3c, Extended Data Fig. 6e

| Authentication | Authentication of cell lines not created in this study was done on the basis of the expected phenotype of the line (PMID: 32029894) |

| Mycoplasma contamination | No test was needed since only S. cerevisiae strains were used |

| Commonly misidentified lines (See ICLAC register) | No commonly misidentified cell lines were used |